Virtual Tide Gauges for Predicting Relative Sea Level Rise

Rhys Hawkins[1] , **Laurent Husson[2]** , **Gaël Choblet[3]** , **Thomas Bodin[1]** , and **Julia Pfeffer[4]**

[1]Laboratoire de Géologie de Lyon Terre, Planètes, Environnement, Université Lyon 1, CNRS and Ecole Normale Supérieure de Lyon, Lyon, France, [2]Université Grenoble Alpes, CNRS, ISTerre, Grenoble, France, [3]Université de Nantes, CNRS, Laboratoire de Planétologie et Géodynamique, Nantes, France, [4]Research School of Earth Sciences, Australian National University, Canberra, ACT, Australia

Abstract We present a Bayesian method to map contemporary rates of relative sea level change using a joint inversion of vertical trends from tide gauges, GPS time series, and satellite radar altimetry measurements. Tide gauge measurements constrain rates of relative sea level change on decadal to secular time scales at a few hundred sites sparsely distributed along coastlines. Predicting the rates of relative sea level change from historical tide gauge measurements is difficult due to the paucity and uneven distribution of sites with high quality records. Since the late twentieth century, deployments of GPS stations have enabled accurate determination of the rates of vertical land motion. A series of satellite radar altimetry missions provide continuous and global monitoring of geocentric sea level changes since the launch of TOPEX/Poseidon in 1992. By combining these three observations types into a single Bayesian inversion, we construct continuous maps of rates of relative sea level change, geocentric sea level change, and vertical land motion assuming linear trends, with robust estimates of uncertainties at regional scales. Cross-validation tests show that reliable predictions of relative sea level changes are still provided where only GPS and satellite altimetry data are used, suggesting this method is viable for studying potential sea level risk for communities where historical tide gauge data are not available. Our results provide spatially and temporally consistent estimates of the various contributions to relative sea level changes.

1. Introduction

Sea level rise is of grave concern due to its potential impact to coastal communities, where a large proportion of the world's population resides (Cazenave & Cozannet, 2014; Church & White, 2011). This has motivated a variety of research into recent and historic sea levels to obtain robust estimates on the varying contributions to modern day rates of relative sea level (RSL) change. As RSLs increase and further impinge on coastal communities, methods for predicting future rates of sea level rise are vital for risk mitigation and planning.

RSL is the sea surface height observed from a reference point on land and is affected by changes in the geocentric sea level (GSL) (Gregory et al., 2019), sometimes called absolute sea level, and vertical land motions (VLM) with respect to a geocentric reference frame, such as $RSL = GSL - VLM$ (e.g., Wöppelmann and Marcos, 2016; Rovere et al., 2016; Pfeffer and Allemand, 2016). VLM and subsequent RSL changes are driven by a broad range of geophysical, climatic, and anthropogenic processes (Conrad, 2013; Pfeffer et al., 2017). Viscoelastic relaxation of the Earth's mantle in response to the growth and melting of ice sheets, or glacial isostatic adjustment (GIA), leads to a complex pattern of uplift or subsidence, for example, large uplift rates where ice sheets were previously residing (Last Glacial Maximum ∼ 25, 000 years ago) and significant subsidence of the sea floor due to addition of freshwater in the oceans (Lambeck & Johnston, 1998; Peltier, 1998; Peltier & Andrews, 1976). Over time scales relevant for estimating contemporary sea level rise, the impact of GIA is approximately linear in time but spatially varying, with generally larger VLM at high latitudes, for example, North America or Fennoscandia (Johansson et al., 2002; Milne et al., 2001).

Mantle convection and plate tectonics can also contribute to VLM across various time scales. On very short time scales, the dramatic release of stress in the form of an earthquake can cause sudden localized VLM, which for large earthquakes can be in the order of tens of centimeters (Yagi & Fukahata, 2011). While such events are episodic in nature and unpredictable, over multidecadal times scales, interseismic tectonic processes contribute to a more gradual creep in VLM (Smith-Konter et al., 2014) that can contribute to slow (and therefore arguably predictable) changes in RSL. On longer time scales, plate tectonics and mantle flow distorts the surface of the Earth at long wavelength and alters GSL (e.g., Husson & Conrad, 2006).

Mass redistribution by erosional and depositional processes can also change the height of land surfaces near coastlines and, on longer time scales, reshape oceanic basins. In addition, human influences can cause local subsidence and uplift; for example, extraction of ground water for consumption and irrigation and oil and gas extraction both tend to produce measurable subsidence of surrounding land. A summary of the range of these effects appears in Pfeffer et al. (2017, Table 4).

In addition to the local to regional variability induced by VLM, tide gauges (TG) measure an elevation in global mean sea level varying from about 1 mm/year in the early twentieth century (Dangendorf et al., 2017; Hay et al., 2015) to about 3 mm/year at present day (Chen et al., 2017; Dieng et al., 2017; Nerem et al., 2018). This rise is a consequence of global warming induced by increased greenhouse gas emissions, causing glaciers and ice sheets (e.g., Greenland and Antarctica) to melt and the ocean to expand as seawater warms and its density decreases (e.g., Church et al., 2013; Horton et al., 2018; Rignot et al., 2011). While dominated by land-based ice melt and thermal expansion, changes in global mean sea level are also impacted by terrestrial water exchanges, causing a net drop in sea level in the order of 0.1 mm/year (e.g. Cazenave & Palanisamy, 2018). However, the rise in mean sea level is far from being uniform in space and time with satellite radar altimetry (SRA) measurements providing observations of regional GSL changes in the order of ± 10 mm/year over the past 25 years (Church & White, 2011; Legeais et al., 2018).

Regional GSL changes are primarily due to the dynamic variations of the ocean-atmosphere system, redistributing heat and salt and water masses heterogeneously within the ocean basins (e.g. Stammer et al., 2013). The mechanisms forcing the ocean variability are generally associated with (i) wind stress, (ii) ocean-atmosphere heat exchanges, and (iii) freshwater exchanges with the atmosphere and continents (Köhl & Stammer, 2008; Lombard et al., 2009). Combined together, these factors result, for example, in climate modes (e.g. Han et al., 2017) shown to influence sea levels across the Pacific, Atlantic, Indian, and Southern Oceans at interannual to multidecadal time scales (Church & White, 2011; Jevrejeva et al., 2006; Pfeffer et al., 2018). Local changes in air pressure (i.e., storm surges, inverse barometer [IB]) also affect sea levels measured at various time scales by SRA and TG. Finally, regional sea level changes (i.e. sea level fingerprints Clark et al., 2002) also result from the adjustment of water masses to varying ice loads in Greenland, Antarctica, and glaciers through gravitational, elastic, and rotational effects (Mitrovica et al., 2001). This spatial variability, both in GSL and VLM, is an important consideration for predictions of future changes in coastal sea levels (RSL).

Previous analyses incorporating TG and SRA have been used to study mean sea level rise due to anthropogenic climate change. For example, Church et al. (2004) examined regional patterns of sea level rise over the twentieth century using recent global observations from SRA combined with TG covering a long time series, at a small number of sites, to infer past sea level. In another example Church and White (2011) used TG data with GIA corrections combined with SRA observations to infer globally averaged sea level rise. More recently, historical sea level changes were reconstructed from the assimilation of TG measurements with physical models of the ice melt (i.e., sea level fingerprints) and ocean dynamics (i.e., climate models), leading to lower rates of sea level rise in the first half of the twentieth century (Hay et al., 2015).

As the number and length of GPS deployments increased, VLM observations have been used to correct TG and place historical sea level measurements in a vertically stable reference frame (Bouin & Wöppelmann, 2010). Pfeffer and Allemand (2016) performed a joint analyses of TG, GPS, and SRA to assess the impact of VLMs on recent sea level changes measured at the coast. This study led to the identification of a few hundred sites shown to be particularly vulnerable to the coastal hazards associated with sea level rise because of land subsidence. The impact of VLMs on historical sea level reconstructions based on TG analysis was tested by Dangendorf et al. (2017), who found that correcting TG using VLM derived from GPS data considerably decreases the rates of sea level rise recovered over the first half of the 21st century. These results were in agreement with Hay et al. (2015), although the techniques employed and reasons invoked differ largely. A limit of this approach is that GPS measurements are rarely colocated with TG. Differences in VLM between the TG and GPS sites may therefore introduce spurious acceleration or deceleration in historical sea levels, which may in turn be misinterpreted as the ocean response to climate change (Featherstone et al., 2015).

A key limitation of studies involving TG is their sparse spatial distribution. In contrast, the changes in ocean surface height have been continuously and globally monitored since the launch of TOPEX/Poseidon in August 2002 (Bosch et al., 2014; Fu and Cazenave, 2000; Legeais et al., 2018). In certain parts of the globe, GPS arrays have been installed at often higher densities than TG. Hence, rather than predicting RSL rise

using point estimates, here we propose solving for spatial models (2-D surfaces) of RSL rise constrained jointly by TG and GSL inferred from SRA and VLM inferred from GPS observations. With this method we show in cross-validation examples that RSL can be reliably inferred in regions where TG coverage is sparse but GPS coverage is sufficient. Our joint inversion approach may provide a tool to investigate risks associated with sea level rise in regions where TG data coverage in the past has been insufficient. However, we acknowledge that the assumption of linear trends may result in an underestimation of future sea level rise in regions of high acceleration (Chen et al., 2017; Dieng et al., 2017; Nerem et al., 2018).

2. Data

As our method makes use of linear trends of vertical rates from three distinct observation techniques, care must be taken in the selection of appropriate time periods due to variability of these rates and record lengths. For the three types of time series data, we have attempted to select overlapping time periods as near as possible while ensuring accurate estimation of trends. Variations in GSL are measured by SRA since 1992. Variations in RSL are measured at TG with a highly variable starting record year, some predating 1900. Observations of VLM are obtained from the Median Interannual Difference Adjusted for Skewness (MIDAS) data set (Blewitt et al., 2015) with the earliest time series data commencing in 1996.

Here, we estimate linear trends in GSL, RSL, and VLM over the 1998 to 2017 time period using a joint inversion of SRA, TG, and GPS data. We only considered SRA data from 1998 onward, because of the significant bias drift spotted in the early altimetry record, particularly for the Topography Experiment - Positioning, Ocean, Solid Earth, Ice Dynamics, Orbital Navigator (TOPEX-Poseidon) mission (Watson et al., 2015). To be consistent with the altimetry data, we selected TG data during the same time period (1998–2017) and ensured on overlap in time of at least 75% for the GPS measurements.

As our focus is limited to the recovery of semicontinental scale and bidecadal features of sea level change, many of the choices below are motivated by a desire to reduce the influence of short-term fluctuations. These choices are somewhat arbitrary and may not apply for studies whose focus includes shorter-term trends or are restricted to smaller regions impacted by complex or fragmented VLM.

2.1. Tide Gauges

For the estimates of RSL, we use a similar procedure as used by Choblet et al. (2014) for the estimate of linear trends and uncertainties but with different selection criteria. In summary, monthly data were downloaded from the Revised Local Reference of the Permanent Service Mean Sea Level (PSMSL) (Woodworth and Player, 2003; Holgate et al., 2013).

We applied an IB correction on the monthly RSL data using the European Centre for Medium-Range Weather Forecasts Reanalysis (ERA) Interim reanalysis (Dee et al., 2011) to estimate atmospheric pressure variations. The IB correction is equivalent to the Dynamic Atmospheric Correction (DAC) at periods longer than 20 days (Pascual et al., 2008, see table 5). The DAC is defined as the sum of IB at low frequencies (periods > 20 days) and a barotropic model at high frequencies (periods < 20 days) (Carrère and Lyard, 2003; Carrère et al., 2016). Given that identical atmospheric pressure (ERA Intermi reanalyses) estimates are used here, the atmospheric corrections applied to tide gauge (IB) and SRA (DAC) measurements are assumed consistent for the study period (1998–2017).

We estimate the rate of RSL change by least squares fitting of a trend to the historical TG measurements. We do this only for records between 1998 and 2017. We consider only stations that have more than 3 years of data in this recent era. For each TG station, we obtain the estimated RSL rate in mm/year with an error estimated through the standard linear regression error estimate of the slope.

Any choice of time period for TG data results in a trade-off between using a shorter time series to obtain more contemporary estimates of RSL rates and using a longer time series to reduce uncertainties in trend estimates caused by, for example, interannual and decadal variability (Douglas, 1992). We have chosen the period from 1998 to 2017 for our TG data to be contemporary with our other observations while acknowledging that this increases the uncertainty of our TG linear trend estimates.

2.2. GPS

For GPS measurements of VLMs, we use the MIDAS data set (Blewitt et al., 2015) and follow the procedure described by Husson et al. (2018). VLM trends and uncertainties produced by MIDAS are used directly. We

remove VLM rates with magnitude greater than 30 mm/year as these generally represent deformation that is coseismic or of man-made origin (Pfeffer et al., 2017). Records shorter than 2 years and with uncertainties larger than 2.0 mm/year are removed. Unreliability of an individual station is estimated by the ratio of the duration of good observations to the station's lifetime. When this ratio is less than 10%, the individual station is considered unreliable and is removed. MIDAS trends are estimated over an individual station's lifetime, which may not overlap our time period of interest. An extra criterion is enforced, whereby at least 75% of a station's lifetime must be within our time period of interest, that is, the linear trend estimated by MIDAS occurs predominantly between 1998 and 2017.

The MIDAS data set removes episodic discontinuities in VLMs and attempts to estimate long-term trends. By using this data set and removing large rates, assumed to be associated with local processes, our aim is to form predictions based on longer-term VLM trends. For tectonically active regions such as Indonesia and Japan, a different approach at a smaller scale would be needed to account for potentially large magnitude, small spatial wavelength, and temporally nonlinear VLMs which can introduce errors of up to 0.4 mm/year when unaccounted for using linear trends (Klos et al., 2019). As the GPS time series data increases in length, more complex predictions could be made about future land motions. However, our intention is to produce a conservative estimate of VLMs at semicontinental spatial scales.

2.3. Satellite Radar Altimetry

The last data type used in this study is SRA. We use the gridded data product monthly mean sea level anomaly maps produced by the Copernicus Marine and Environment Monitoring service (Copernicus Marine and Environment Monitoring Service, 2018). Data were downloaded from 1998 to the end of 2017, and an estimate of GSL rate of change and uncertainty was estimated for each valid grid point using standard linear regression techniques. Grid points where there are less than 12 monthly observations in the time period of interest are removed. We tested using less and more stringent criteria, and these had little impact on the obtained trends. Similarly to GPS observations, if the magnitude of the estimated GSL rate is larger than 15 mm/year, the observation is removed as an outlier.

In principle, RSL can be inferred directly from the combination of observations of GSL from satellite altimetry and VLM from GPS. A complication arises from a current weakness of SRA observations near shore lines due to spurious reflections from land (Gommenginger et al., 2011). While the gridded data products generally only provide GSL estimates for grid points far from land masses, we additionally remove any grid point that is within 20 km of any landmass (both for oceans and enclosed/semienclosed seas). While this clearly reduces data coverage of the sea level measurements near the coast, it was deemed preferable to potentially including spurious land reflections that could adversely affect results.

The data from Copernicus - Marine Environment Monitoring Service is of a sufficiently fine resolution (a quarter degree) to record sea level changes caused by ocean and climate dynamics, at short temporal and space scales (e.g., eddies). Such localized features are not the focus as we wish to estimate larger-scale trends. In an attempt to reduce the impact of small-scale length features on our estimates of RSL, we apply a Gaussian filter with standard deviation of 1° followed by decimation to a 1° resolution set of observations.

2.4. Summary

In summary, we have compiled three independent data sets of point-based estimates of RSL, VLM, and GSL trends covering the time period 1998 to 2017. The spatial distribution of these data are shown in Figure 1 with a summary of the data selection criteria and the numerical count of data points in each study region shown in Table 1.

3. Method

The method we propose is applied to a 2-D region of the Earth within which we have a set of observations for our three data types. We parameterize this region with two independent continuous surfaces of GSL rate and VLM rate. The RSL rate can be easily predicted from difference of these two surfaces.

We use a Bayesian transdimensional approach, whereby the model complexity is dynamically adapted, to produce posterior probability distributions on the likely RSL rates given the observations. We provide an overview of the approach here, but details appear in Hawkins et al. (2019). The general Bayesian approach (Brooks et al., 2011; Gelman et al., 2004) uses Bayes theorem
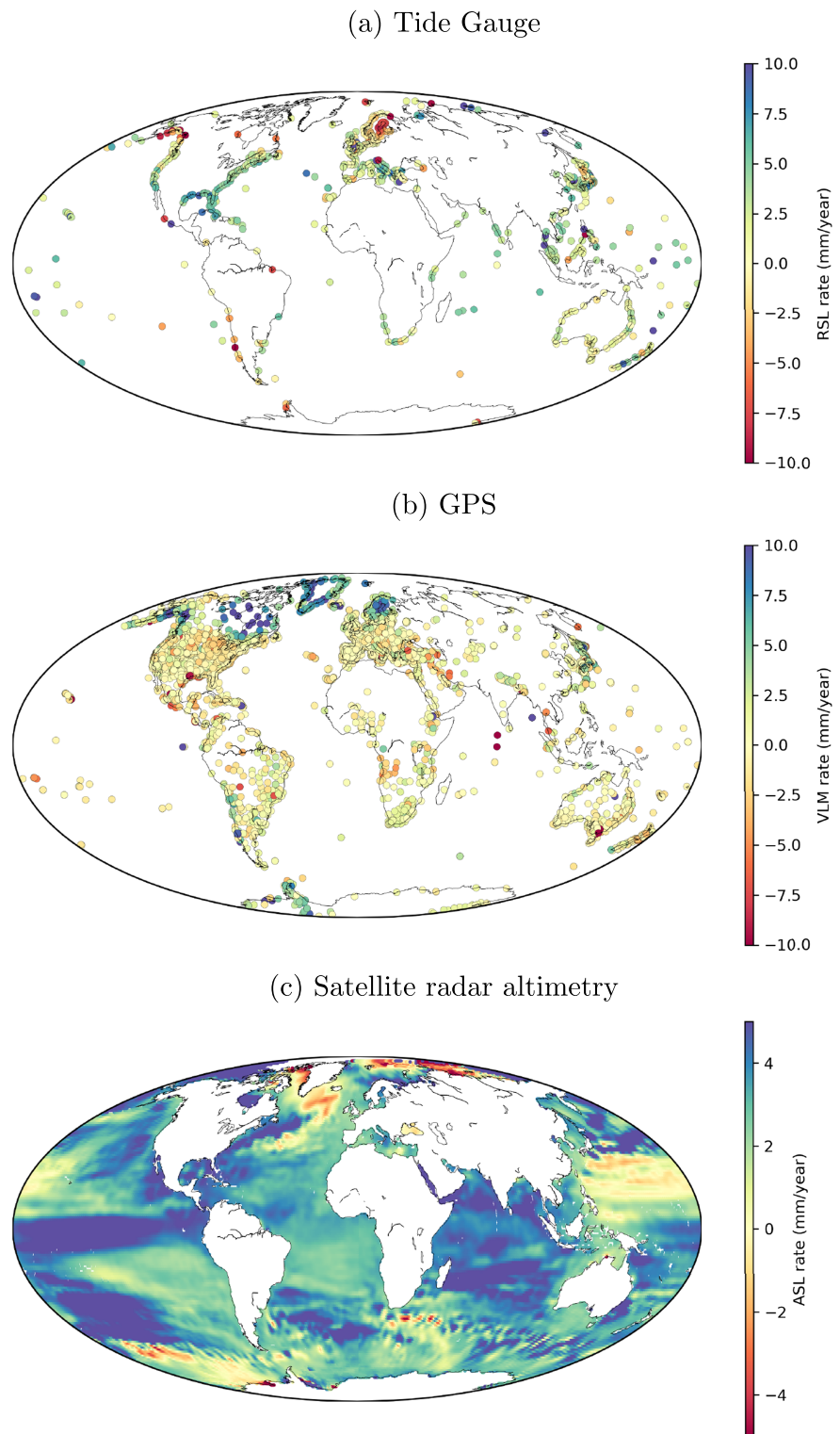
Figure 1. A global view of the data used in this study. (a) The relative sea level (RSL) rates measured at quality controlled tide gauge (TG) stations obtained from PSMSL. (b) the vertical land motion (VLM) rates measured from GPS, obtained from the MIDAS database. (c) The geocentric sea level (GSL) rate obtained from satellite radar altimetry (SRA) data.

Table 1

Summary of the Selection Criteria Used to Remove Observations That Are Not in the Relevant Period or Determined To Be Outliers for Each of the Data Types and Number of Data Points for Each Data Type and Region in This study

		Selection Criteria	
	TG	GPS	SRA
Temporal	At least 3 years of data between 1998 and 2017	At least 2 years of data and at least 75% of total recording time between 1998 and 2017	At least 12 data points between 1998 and 2017
Magnitude	Within ±15 mm/year	Within ±30 mm/year	Within ±15 mm/year
Uncertainty	Error less than 3.0 mm/year	Error less than 2.0 mm/year	Error less than 1.5 mm/year
Other	No errors flagged and less than 10 days missing per month	Ratio of at least 10% of recording time to lifetime	Points within 20km of land removed
		Data Counts	
	TG	GPS	SRA
Africa	71	683	3,843
Asia	179	1,030	2,121
Australia	63	296	1,340
Europe	241	2,847	1,070
North America	154	4,756	3,286
South America	22	287	3,564

$$p(\mathbf{m}|\mathbf{d}, \mathcal{I}) = \frac{p(\mathbf{m}|\mathcal{I})p(\mathbf{d}|\mathbf{m}, \mathcal{I})}{p(\mathbf{d}|\mathcal{I})}, \tag{1}$$

where $\mathbf{m}$ is the vector of model parameters, $\mathbf{d}$ is the vector of observed data, and $\mathcal{I}$ represents additional prior information in the formulation of the problem, such as the parameterization (Malinverno, 2002; Hawkins et al., 2019). The posterior probability distribution, $p(\mathbf{m}|\mathbf{d}, \mathcal{I})$, is estimated from a product of the prior, $p(\mathbf{m}|\mathcal{I})$, and the likelihood $p(\mathbf{d}|\mathbf{m}, \mathcal{I})$ using a hybrid of Markov chain Monte Carlo (McMC) (Mosegaard and Tarantola, 1995; Sambridge & Mosegaard, 2002) and Hamiltonian Monte Carlo (HMC) techniques (Duane et al., 1987; Neal, 2011). The term $p(\mathbf{d}|\mathcal{I})$, often called the evidence or marginal likelihood, is a normalization term and not required in this study as we do not consider alternate models.

The two surfaces are each parameterized as a variable set of mobile nodes located within the region of interest and their associated value represent a rate of sea level or VLM. The transdimensional inversion treats the number of nodes, that is, the complexity of the surface, as an unknown for which posterior inference is also sought. The software provided by Hawkins et al. (2019) allows selection of three different schemes for how the nodal points are interpolated to construct a 2-D surface. In this study, we have chosen a Delaunay linear interpolation for the recovery of smooth features, namely, maps of regional GSL (without highly localized weather and ocean current anomalies) and VLM due to GIA and longer-term tectonic deformations.

The model can be written mathematically as a joint vector of the sea and land rate models

$$\mathbf{m} = \begin{bmatrix} \mathbf{m}_{\text{GSL}} \\ \mathbf{m}_{\text{VLM}} \end{bmatrix}, \tag{2}$$

and similarly for the data

$$\mathbf{d} = \begin{bmatrix} \mathbf{d}_{\text{SRA}} \\ \mathbf{d}_{\text{GPS}} \\ \mathbf{d}_{\text{TG}} \end{bmatrix}, \tag{3}$$

where the abbreviated subscript "SRA" refers to satellite radar altimetry observations, "GPS" refers to GPS observations of VLM, and "TG" to tide gauge observations. With these definitions of model and data vectors, a joint likelihood function can be formed using

$$p(\mathbf{d}|\mathbf{m}, \mathcal{I}) = p(\mathbf{d}_{\text{SRA}}|\mathbf{m}_{\text{GSL}}, \mathcal{I})p(\mathbf{d}_{\text{GPS}}|\mathbf{m}_{\text{VLM}}, \mathcal{I})p(\mathbf{d}_{\text{TG}}|\mathbf{m}_{\text{GSL}}, \mathbf{m}_{\text{VLM}}, \mathcal{I}). \tag{4}$$

For each of the likelihood functions above, we assume an independent Gaussian likelihood function. For example, the likelihood function of the satellite altimetry data is

$$p(\mathbf{d}_{\text{SRA}}|\mathbf{m}_{\text{GSL}}, \mathcal{I}) = \frac{1}{\sqrt{2\pi}\prod_{i-1}^{N_{\text{SRA}}} \lambda_{\text{SRA}}\sigma_{\text{SRA},i}} \exp\left\{ -\frac{1}{2}\sum_{i=1}^{N_{\text{SRA}}} \frac{(G(\mathbf{m}_{\text{GSL}}) - \mathbf{d}_{\text{SRA}})^2}{(\lambda_{\text{SRA}}\sigma_{\text{SRA},i})^2} \right\}, \tag{5}$$

where G is the forward model for predicting observations based on the model which in this case is the Delaunay parameterization with a linear interpolant, and σ is the estimated error in the observations obtained as previously described in the data section. Lastly, the λ term is a hierarchical error scaling factor which is also inverted for (Malinverno and Briggs, 2004; Choblet et al., 2014; Hawkins et al., 2019). An independent hierarchical scaling parameter is used for each class of observation for two purposes: first it is able to account for under or over estimation of data errors. For example, it will account for theoretical errors in forward modeling due to the inability of the interpolated Delaunay surfaces to represent the true surfaces. Second, by having independent hierarchical error terms, the inversion automatically adjusts the relative importance of each of the observation types to the final solution.

We implemented an extension to software provided by Hawkins et al. (2019) through the general interface provided. The software uses HMC for sampling the posterior probability density of the values of GSL and VLM trends, and reversible jump McMC for changes to the underlying Delaunay triangulated mesh; this

includes both changes to the location of nodes and adding and removing nodes to increase or decrease the complexity of the model to represent the data.

For the inversion presented here, we use statistics from multiple independent parallel chains which are subsequently combined into a single ensemble of plausible models upon which statistical inference is performed. The independent chains are also used as a gauge of chain convergence through computing the Gelman-Rubin statistic on hyperparameters as a proxy of convergence (Gelman & Rubin, 1992; Hawkins et al., 2018). The simulations for each of the joint inversions also uses Parallel Tempering (Earl & Deem, 2005; Sambridge, 2014) to help prevent chains from becoming stuck in local modes and to ensure adequate mixing of the Markov chains.

For the prior on GSL and VLM rates, we use a uniform prior within ±10 mm/year. A Jeffreys prior is used on the hierarchical error scaling parameters, and a discrete uniform prior between 1 and 500 is used on the number of nodes for the two regional models (GSL and VLM). HMC and McMC proposal parameters are tuned to obtain near optimal acceptance rates (approximately 80% for HMC and 25% for McMC). We use 48 parallel independent chains at four logarithmically spaced temperatures between 1 and 5 for Parallel Tempering leaving 12 independent chains upon which statistical inferences are performed. We typically simulate chains for 1,000,000 iterations and process only the last 500,000 which are then thinned by taking every tenth model to create an ensemble of 1.4 million models (28 times 50,000).

For comparison, we also perform inversions with no TG data and with TG data alone. When inverting only TG, we invert directly the RSL surface using the standard regression module of the software with a linear Delaunay parameterization (Hawkins et al., 2019).

4. Results

The outcomes of the inversions are grids of posterior probability density functions (PDFs) at all locations, giving the rates of GSL, VLM, and RSL. For convenience and visualization purposes, we present these results by extracting maps of the ensemble mean and standard deviations, as well as 2-D profiles along coastlines, showing the full PDFs.

We have run inversions on six regions on the Earth covering major land masses. For brevity and to highlight the salient aspects of this method, we show and discuss results in detail only for two contrasting regions: Europe where data coverage is excellent and South America where in general there exists a good coverage of GPS observations and a relatively poor coverage of TG observations. Other regional inversions (North America, Asia, Africa, and Australia) are briefly presented below in summary, with detailed figures in the supporting information.

For all regions, we provide all digital grids for GSL, VLM, and RSL obtained in this study.
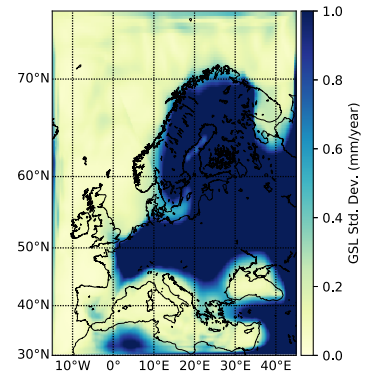
4.1. Europe

We use Europe as a demonstration region, primarily because the network of TG and GPS stations is denser in Europe than anywhere else (Figure 1). Monitoring sea level has a long history in the European region with several TG in continuous operation for a century or more. In the time period selected, 241 TG are available. In Europe, TG stations are seldom separated by more than a few hundred kilometers, with exceptions in the northernmost latitudes, the Black sea and the Middle East. Similarly, permanent GPS stations have been deployed for many decades in Europe and provide a long time series of geodetic observations (2,847 GPS are available for the selected time period). The combination of long time series and density of stations (TG and GPS) means that the European region offers thorough coverage for a joint inversion and represents a best case scenario for our approach among the regions of the Earth.

From the joint inversion of linear trends of TG, GPS, and SRA, we obtain 2-D posterior distributions for GSL, VLM, and RSL from which ensemble means are shown in Figures 2a, 2c, and 2e, respectively. From these figures, GSL predictions generally vary between 0 and the 5 mm/year. Predictions for VLM, in Figure 2c, are very close to those obtained using GPS only (Husson et al., 2018) as the network is very dense allowing robust predictions. It strikingly reveals the postglacial rebound uplift of Fennoscandia (Milne et al., 2001; Johansson et al., 2002), centered in the north of the Baltic sea, as a consequence of the Holocene deglaciation. Since the amplitude of spatial variations of GSL are smaller than that of VLM variations, RSL predominantly displays a mirror image of VLM, offset by the ~3 mm/year of mean sea level rise (WCRP Global Sea Level Budget
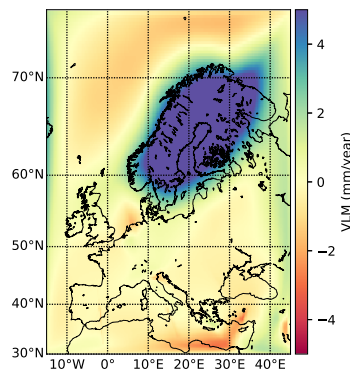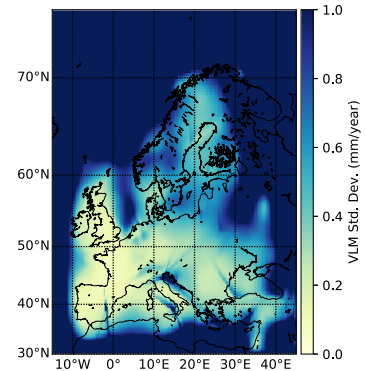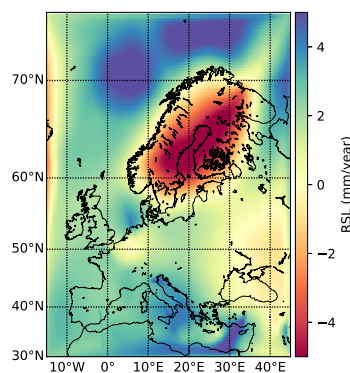
(a) GSL Rate Mean
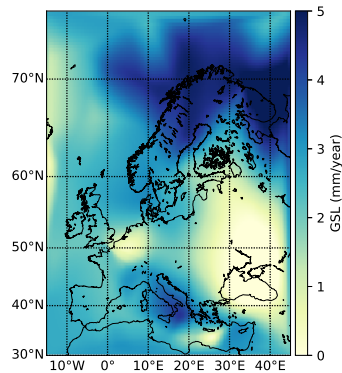
(b) GSL Rate Std. Dev.

(c) VLM Rate Mean

(d) VLM Rate Std. Dev.

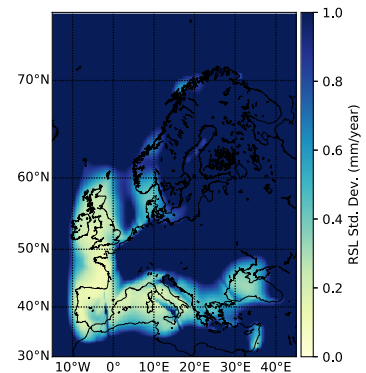(e) RSL Rate Mean

(f) RSL Rate Std. Dev.

Figure 2. Ensemble mean plots for (a) GSL, (c) VLM, (e) RSL and standard deviation plots for (b) GSL, (d) VLM, (f) RSL for the joint inversion of all data types for the European region.

Group, 2018). Uplifting Fennoscandia dominates, and RSL peaks to maximal rates of −5 to −6 mm/year in the north of the Baltic sea. In comparison to earlier spatial maps of RSL that only considered TG (Choblet et al., 2014), the maps produced here are in good agreement but generally smoother owing to inclusion of better constrained observations (i.e., GPS and SRA).

At smaller scales, features are reproduced such as subsidence the Po plain (∼1 mm/year) and uplift in the Alps (less than 1 mm/year on average). In the Aegean sea, RSL falls at ∼1 mm/year, while RSL rises in the
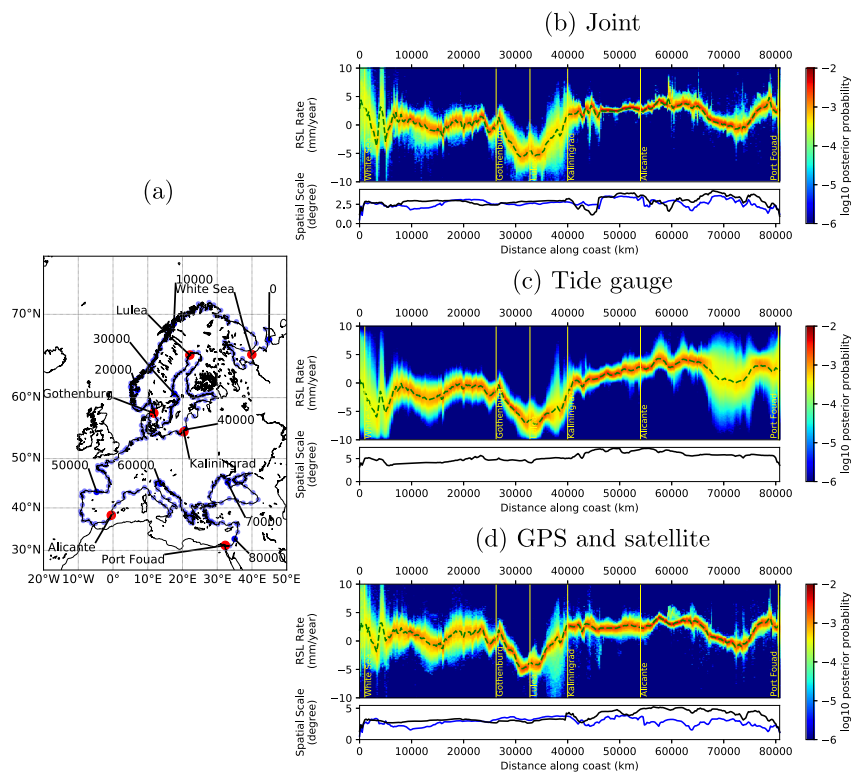
Figure 3. (a) Location of virtual tide gauges indicated by blue points, with numerical labeling indicating distance in kilometers from the starting point (0). Red points indicate selected coastal cities. (b) The $\log_{10}$ of the posterior probability distribution of joint inversion of RSL along the coastline in (a). (c) The same as (b) but for an inversion using only tide gauges. (d) The same as (b) but for a joint inversion of SRA and GPS (i.e., no TG). In general, the posterior appears better constrained in this case (narrower posterior width) with the joint inversion in (a). Under each posterior plot we show the mean spatial scale along the coastline path, a proxy for resolution, with black representing the VLM or RSL model in (b) and blue representing the GSL model.

adjacent Peloponnese and Anatolia, at 2–4 mm/year. However, although the signal nicely delineates the extent of the Aegean sea, centered on the Cyclades, the standard deviation is high. This region has a high degree of tectonic activity (e.g. Angelier et al., 1976), which given our choices of fitting linear trends may result in discrepancies between TG and GPS observations and potentially cause high uncertainties in this region. Model predictions of GIA (e.g., Lambeck & Purcell, 2005) conversely indicate RSL rise in the Aegean sea. In the Middle East, there are only few TG available, yet the uncertainty is quite low owing to the the many nearby GPS stations.

Since our method inverts for a contiguous surface across the prescribed domain, even where there is no data coverage, GSL and RSL changes are displayed onshore and VLM offshore. Of course, uncertainties quickly increase away from regions of data coverage as can be seen in ensemble standard deviations shown in Figures 2b, 2d, and 2f. We note that in all cases, rates near the shoreline are almost systematically well constrained. This is explained by the fact that at the shoreline, all three data sets can contribute to constraint of the model. Hence, the lack of a tide gauge at a location can be supplemented in part by nearby observations of VLM from GPS observations and GSL change from SRA observations.

Arguably, a more useful approach to examining RSL change is to investigate trends along coast lines rather than with 2-D maps. With our approach, we construct a series of *Virtual Tide Gauges* along a contiguous coastline as shown in Figure 3a. In Figure 3a, the path starts at the coast near the White Sea in the northeast at the point indicated with 0 and proceeds continuously along the coast, through the Baltic and Mediterranean seas, to the southeast near Port Fouad. At intervals of 10,000 km, we indicate regular distances along this path and mark some cities with red points. These virtual tide gauges allow a regular profile of RSL along the European coastline to be constructed in Figure 3b, with generally narrow credible intervals about the

mean value. Only in the White sea, where all data classes have poor coverage, is the spread of the shaded region representing uncertainty larger than ±1 mm/year. These posterior PDFs allow visualization of RSL rates of change and their uncertainties along coastlines at a glance.

Defining the level of resolution in a nonlinear transdimensional problem is difficult and has only recently been addressed for 1-D problems (Menke & Blatter, 2019). Here, we do not consider the resolution as it is mathematically defined in linear inverse theory and represented by a resolution matrix (Backus and Gilbert, 1968; Aki, 1977). Rather, in an effort to quantify the spatial scale of our results, we compute the mean size of triangles (in degrees) for each point of the map. While this is not a direct measure of the smallest scales that can be recovered, it is a reliable proxy except for some pathological cases. For example, a dense sampling of low noise observations of a spatially constant field will be represented by a few triangles resulting in a low spatial scale by this metric. For Europe, we generally have a spatial scale of around 2.5° along the coastline for the joint inversion.

A useful cross-validation experiment is to compare the probabilistic RSL surface obtained from the full joint inversion to results obtained with only tide gauges and results from only GPS and SRA observations. This comparison is shown in Figure 3 where the full joint inversion of the three observations class is shown in Figure 3b with inversions obtained with TG only in Figure 3c and with GPS data and sea surface altimetry (i.e., without tide gauges) in Figure 3d. These results reveal how the combination of SRA and GPS data generally provide similar estimates of RSL rates and can be used to robustly estimate RSL for regions where there are insufficient TG stations. Unsurprisingly, constraint is poor in the case where data from all three observational types are insufficient (e.g., the White sea region). Also note that in this case, the spatial scale is generally improved in the joint inversion compared to the TG only and GPS and SRA inversions.

In regions where the solution is well constrained with small standard deviations, for example, in the Kaliningrad-Alicante coast, the RSL rates are generally in the 2.5–3 mm/year range whereas Choblet et al. (2014) found rates closer to 2 mm/year. This is likely due to this study using more recent data and only including TG records between 1998 and 2017. This increase in rates is broadly in agreement with reported accelerations for global mean sea level rise (Church and White, 2011; Dangendorf et al., 2017).

Along the coast from Alicante to Port Fouad, the TG only inversion displays a large standard deviation. This feature is strongly attenuated in the joint inversion and absent in the GPS/SRA inversion. This is likely due to local tectonic or human induced effects on the TG or inconsistent TG identified by Choblet et al. (2014). In the regions where TG are less abundant, GPS and sea level altimetry are able to effectively overcome the lack of tide gauge information. For example, in the Middle East, virtual tide gauges allow us to predict RSL rise at $\sim 3 \pm 1$ mm/year.

In summary, in the European region we have good coverage of all three data types and the joint inversion produces generally similar predictions to the TG only and to GPS and SRA only inversions. Where TG stations have a low uncertainty (e.g., between Kaliningrad and Alicante or north of Gothenburg), the joint inversion has the lowest uncertainty. Where TG stations are subject to greater uncertainties, the GPS/SRA only inversion can produce slightly lower uncertainties (e.g., between Gothenburg and Kalilingrad or between Alicante and Port-Fouad).
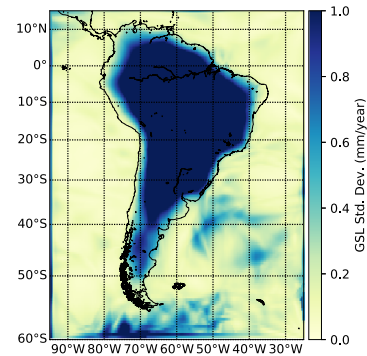
4.2. South America

With reference to Figure 1a, the coverage of tide gauges in South America is sparse compared to that of Europe, (22 TG in South America, compared to 241 in Europe). By comparison to TG in South America, the distribution of GPS stations is denser, with 287 GPS stations in our quality controlled data set for this region. This continental region therefore provides a good example of the performance of RSL rate predictions where tide gauge coverage is poor.

In Figure 4a we can see the GSL rate surface model essentially recovers the grid seen in the global data map in Figure 1c. Broadly, the GSL rates are positive with a larger magnitude anomaly to the south east. VLM shown in 4b, is dominated by uplift along the west coast and in the western part of the Andes. This uplift reaches its maximal values in the Patagonian ice fields, where current rates of melting are causing extremely fast uplift rates (Richter et al., 2016). To the east of the Andes, there is a broad swath of subsidence in the foreland basins. In Figure 4c, RSL rates show a near 0 to positive rate along the west coast north of 20°S as coastal uplift tends to cancel out GSL rise. However, in Patagonia the melting of the ice fields causes
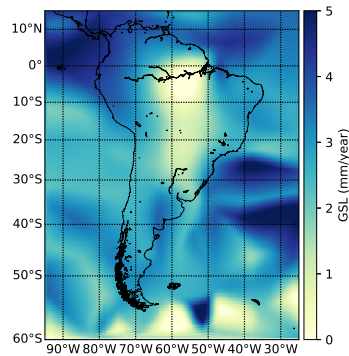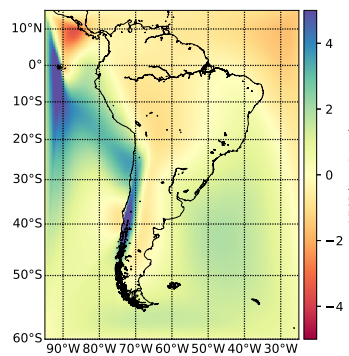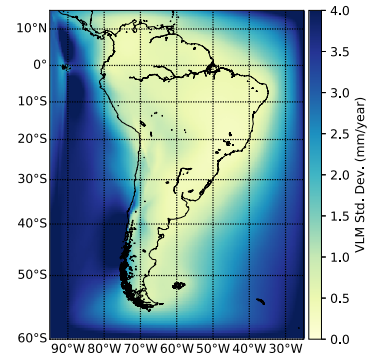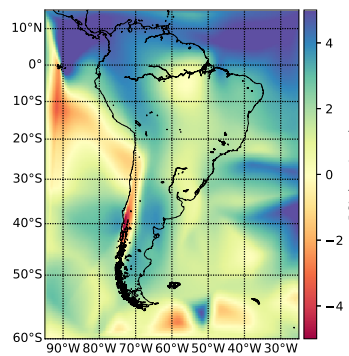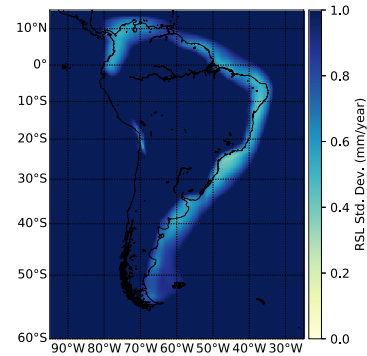
Figure 4. Ensemble mean plots for (a) GSL, (c) VLM, (e) RSL and standard deviation plots for (b) GSL, (d) VLM (f) RSL for the joint inversion of all data types for the South American region.

a net RSL fall at fast rates (up to 5 mm/year). In contrast, along the east coast where VLM are smaller in magnitude, there is a generally small positive change in RSL.

With reference to Choblet et al. (2014), who only examined TG, results shown in Figures 4e and 5b can be compared, keeping in mind that the time series in the current study largely differ in their duration and recovered period. A major difference is in the region around Lima where Choblet et al. (2014) report a large magnitude and highly localized positive anomaly which is not seen in this study. Possible explanations for this discrepancy include all aspects, from a different parameterization, the use of different time periods for
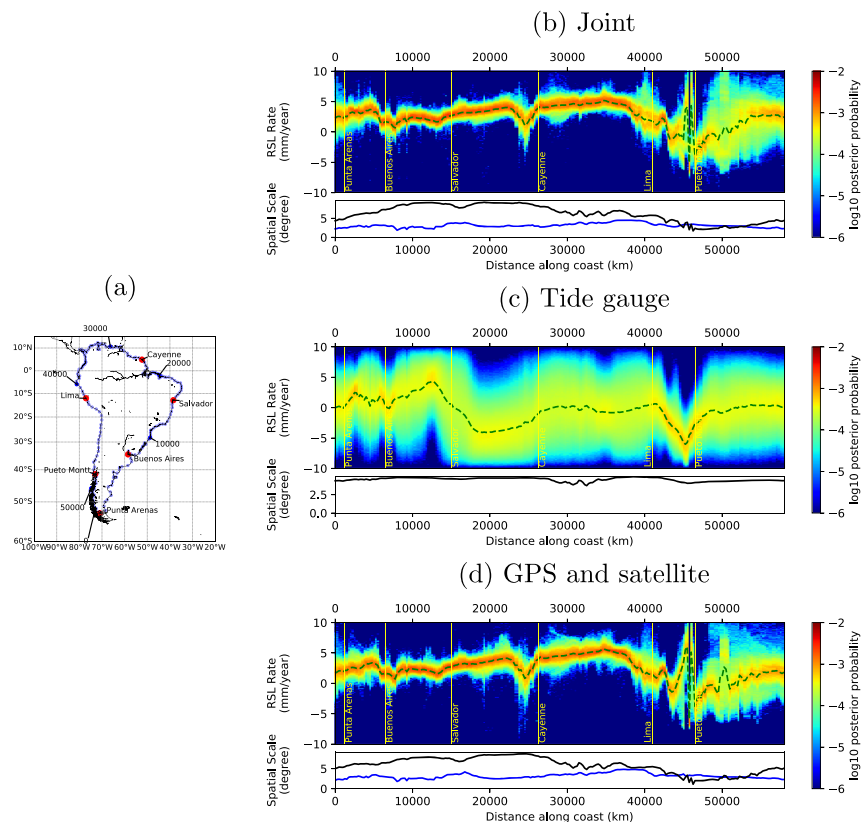
Figure 5. (a) Location of virtual tide gauges indicated by blue points, with numerical labeling indicating distance in kilometers from the starting point (0). Red points indicate selected coastal cities. (b) The $\log_{10}$ of the posterior probability distribution of joint inversion of RSL along the coastline in (a). (c) The same as (b) but for an inversion using only tide gauges. (d) The same as (b) but for a joint inversion of SRA and GPS (i.e., no TG). With only TG, there is very little information due to poor coverage. Under each posterior plot we show the mean spatial scale along the coastline path, a proxy for resolution, with black representing the VLM or RSL model in (b) and blue representing the GSL model.

the tide gauge observations, localized tectonic activity, and, given the proximity to the equatorial Pacific Ocean, El Niño–Southern Oscillation.

The clear picture emerging from Figure 5 is that the estimation of coastal RSL rates in Figure 5c, with TG only, is very poorly constrained compared to the joint inversion and the inversion with just GPS and Satellite observations. This is indicated by the generally smooth mean as a function of coastal distance and wide uncertainties in Figure 5c compared to Figures 5b and 5d. Strong variations in the spatial scale are observed for the joint and the GPS/SRA only inversions, with smaller scale features reported in the region between Pueto Montt and Punta Arenas and a corresponding increase in uncertainties. This suggests that there is a high degree of variability in this region. In comparing Figure 5b and Figure 5d in this region, the addition of TG observations has increased uncertainty and is the result of a single contradictory TG observation of ~ -2 mm/year when nearby GPS/SRA predict $\sim +2$ mm/year (see Figure 2a). For the TG inversion, the model is unconstrained resulting in large uncertainties and paradoxically small spatial scale features.

The results for the full joint inversion Figure 5b and the GPS/Satellite inversion Figure 5d are almost identical owing to the fact that there are few TG and therefore most of the information used for prediction of the RSL at our virtual tide gauge locations comes from GPS and SRA observations.

In summary, the TG coverage alone is not sufficient to predict RSL along the coasts of South America. Instead, our method can provide robust virtual tide gauges by jointly inverting complementary data from GPS and SRA observations.
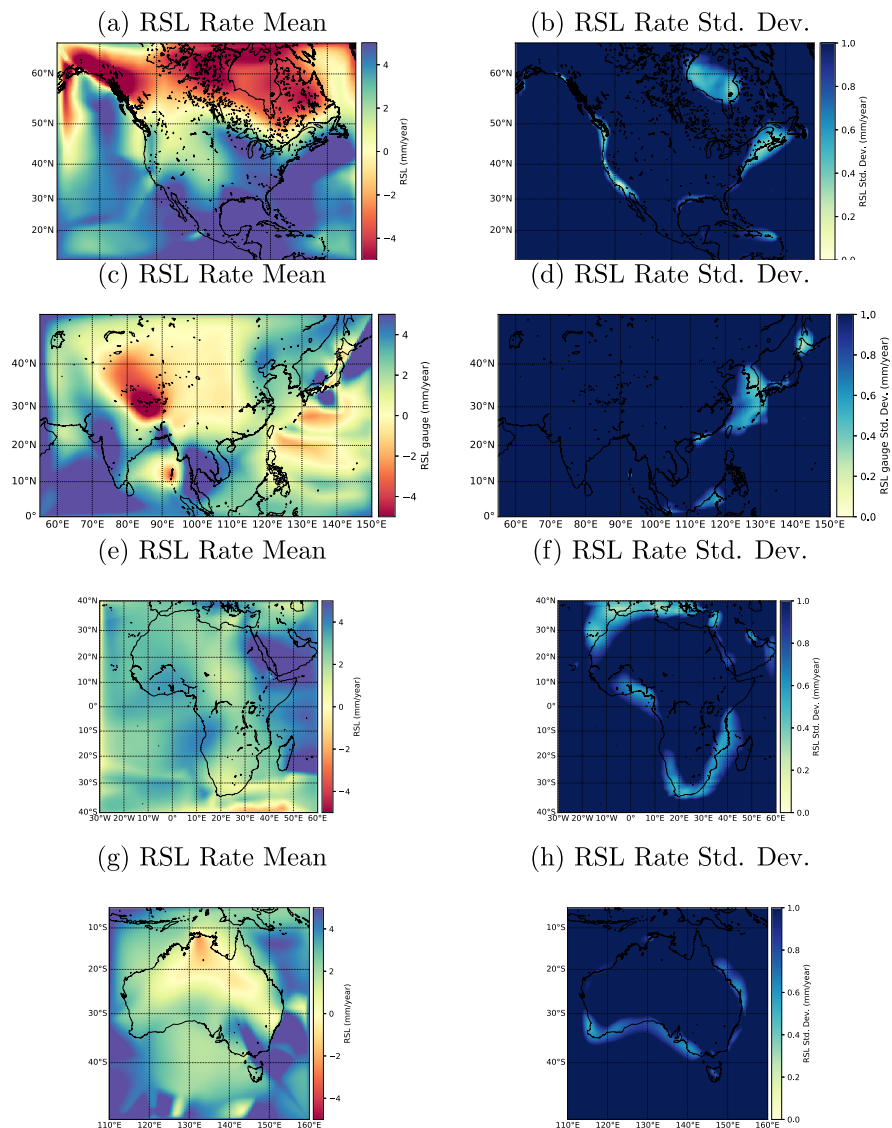
Figure 6. The ensemble mean and standard deviation maps of RSL for the other regions: (a and b) North America, (c and d) Asia, (e and f) Africa, and (g and h) Australia.

4.3. Other Regions

For other major regions of the Earth, we present a brief summary of the results with further plots in the supporting information.

4.3.1. North America

Many aspects of the North American study are analogous to that of Europe. Their sizes, latitude range from mid latitudes to within the arctic circle, and data density, distribution and duration of time series are comparable for the most part (Figure 1). TG are numerous and closely spaced along the coastlines of Canada and conterminous USA, and moderately more sparsely distributed in Mexico and in the Caribbean. Dense arrays of GPS stations exist in USA and Canada, south of the arctic circle although the highest density is located in western, actively deforming areas, and in the eastern half of the continent. GPS station coverage in Mexico and the Caribbean is less extensive. Both trends of TG (Choblet et al., 2014) and GPS data (Husson et al., 2018) clearly delineate the uplifting northern region following its deglaciation. Fast land subsidence, and associated RSL rise in the east coast and in the Gulf of Mexico are also prominently resolved by both data sets independently.

In Figures 6a and 6b we show the ensemble mean and standard deviation maps respectively for the RSL rates in the North American region. The mean map is dominated by large negative RSL rises in the north
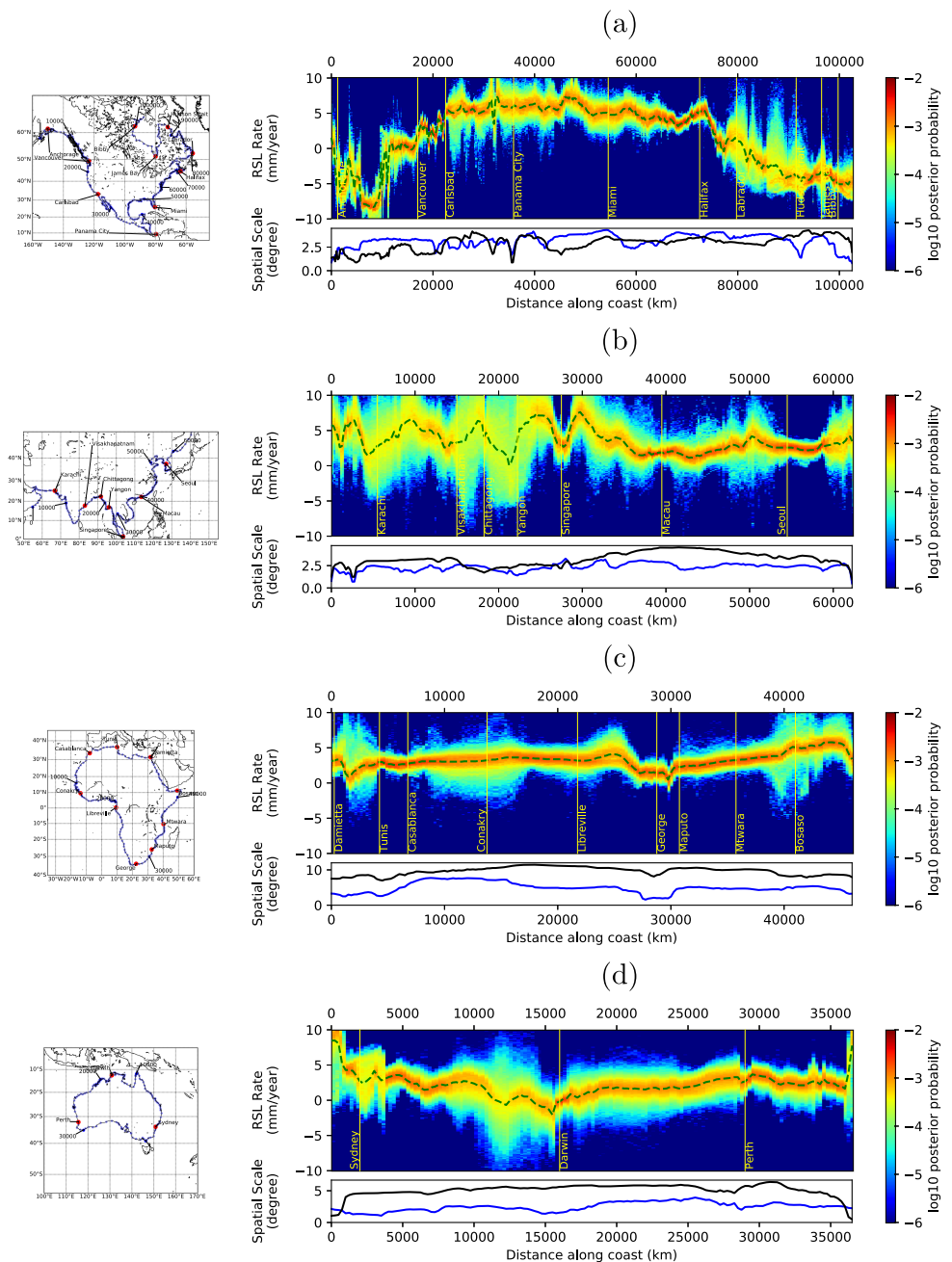
Figure 7. Virtual tide gauge posteriors from the joint inversion of all observations for other regions studied with virtual tide gauge locations to the left. In (a) North America, (b) Asia, (c) Africa, and (d) Australia.

owing to large GIA induced VLMs (Kreemer et al., 2018; Husson et al., 2018), and strong positive rates in the Gulf of Mexico due to land subsidence in the Mississippi delta region. On the east coast our joint inversion recovers rates of RSL of ∼ 4–5 mm/year compared to ∼ 2–3 mm/year on the west coast predominantly due to the influence of GSL rates. In Figure 7a, the posterior shows the more dramatic range of RSL rates (e.g., compared to European results) with rates as low as ∼ −10 mm/year in the north, and as high as ∼7 mm/year in the Gulf of Mexico, with uncertainties that are generally lowest along the east and west coasts of the USA, owing to better coverage of both TG and GPS stations.

Overall, RSL is well resolved along most coastlines of conterminous USA and Caribbean, but the level of constraint on RSL degrades at high latitudes. The joint inversion of the three data sets reduces the uncer-

tainty at all locations, relative to inversions using TG only and GPS and satellite altimetry (see supporting information). At high latitudes, where the data sets become more sparsely distributed, the inversion of TG data only over estimates RSL fall relative to the other inversions. These results demonstrate the potential that virtual tide gauges have in supplementing our understanding of RSL trends globally.

4.3.2. Asia

In the Asian region, the distribution of TG varies considerably (Figure 1) with good coverage in the east (along the coast of China, Korea and Japan), and poor coverage in the west (from the Indian peninsula and further west). Similarly, GPS stations are denser in Japan and in the east than elsewhere. In the west, there is only good coverage of GPS stations in the Himalaya where tectonic signals are well resolved in VLM maps (see supporting information). However, these stations are far from the coast and have little impact in constraining estimates of RSL trends at the coast. Poor data coverage in the west is shown well in maps of RSL standard deviation in Figure 6d where only the Chinese coast, Korean Peninsula, and Japan have low uncertainties.

The RSL map in Figure 6c reveals a pattern dominated by geodynamic processes: Himalayan uplift, subsidence due to sediment loading in the Ganga plain and in the Bengal fan, or in Japan mirroring the transient and laterally variable seismic activity. Note that the apparent RSL fall in the Andaman is obtained from a single GPS station, and hence should be considered cautiously, as the standard deviation is large in this area.

Likewise, in Figure 7b the posterior distribution of the virtual tide gauges along the coastline reflects the uneven data distribution. Much lower uncertainties are obtained for locations near Singapore, in Korea and Russia, where both TG and GPS are numerous, than on the western part of the region, from Myanmar to Pakistan. In this region, a rough signal is apparent in the joint and the GPS/SRA inversions yet not present in the TG only inversion (see supporting information). It involves for example a local maximum in RSL associated to subsidence of the Bengal fan yet the standard deviation is large suggesting more GPS stations would be required to better assess RSL. Conversely in the east, the joint inversion significantly improves the spatial scale by introducing higher spatial frequencies that are not revealed by TG alone. This contrasted behavior, between the eastern and western sides of Asia, demonstrates the added-value of virtual tide gauges, but again, where GPS data coverage is sufficient.

4.3.3. Africa

In the case of Africa, the distribution of TG is biased toward the northern coastline and South Africa with generally poorest coverage on the east and west coastlines. In previous studies using only TG observations, a relatively homogeneous small negative rate of RSL rise was obtained, associated with a large uncertainty (Choblet et al., 2014). Our processing show that with TG only, but more recent data (1998–2017), positive RSL values are obtained (see supporting information). This result is confirmed by the joint inversion of all three data sets (Figure 6e). Inspection of individual TG signals in the period 2011–2017 in the best constrained South African region reveals that a recent increase in TG observations is responsible for this contrasting outcome of the present study, again highlighting the importance of time series selection for this data type.

GPS data are slightly more numerous than TG data owing to the deployment of several GPS networks. These are significant and helpful in some places like in South Africa, where inversion with GPS and SRA (i.e., without TG) confirms that the result obtained for TG only is more reliable than the one presented in Choblet et al. (2014) given more recent data. Yet, the uneven distribution of GPS networks can also produce misleading results: stations are more extensively deployed in the tectonically active regions, like the East African Rift. Since the neighboring east African coastline is less covered, such stations may yield an apparently robust signal. Overall, the benefit of virtual tide gauges is unclear in Africa, and their interpretation requires obvious caution. For the African continent, both TG and GPS data sets are generally too sparse to depict the spatial behavior of RSL rates at the continental scale.

4.3.4. Australia

In the case of Australia, the distribution of TG is dominated on the east coast in large population centers from Brisbane, through Sydney and Melbourne, to Adelaide. Australia's intraplate setting make it relatively tectonically quiet with a slow tilting of the Australian Plate resulting in negative VLMs in the northwest and positive in the southeast (Sandiford et al., 2005; Quigley et al., 2010) but at rates generally smaller than the uncertainties on GPS estimates.
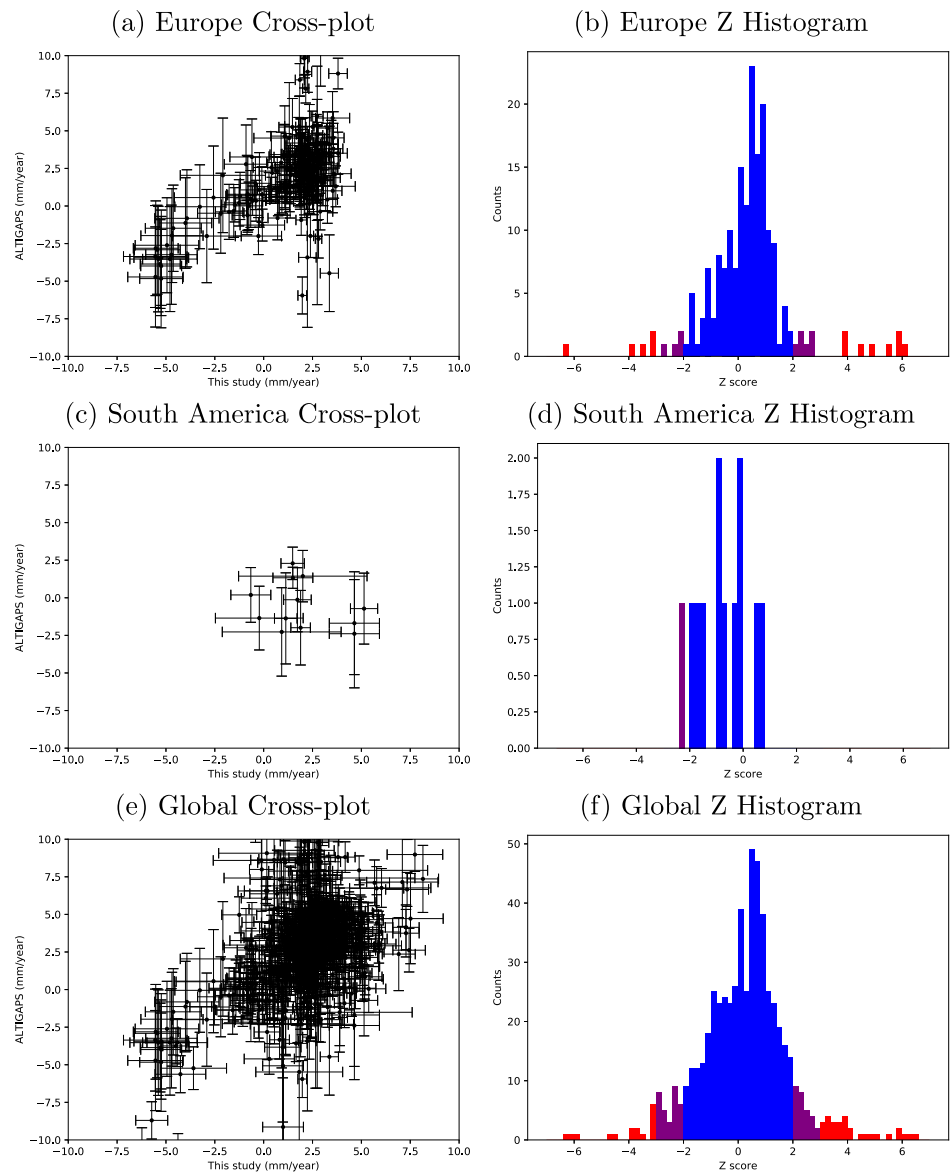
Figure 8. Cross plots between ALTIGAPS values and uncertainties against estimates from the full joint inversion for the European (a), South American (c), and all regions combined (e). The relationship is approximately linear suggesting good agreement between the two independent studies. When considering uncertainties, the *Z* score histograms in (b), (d), and (e) show there are very few observations that disagree (red shaded).

This leads to a mostly flat surface of VLM, as revealed by GPS data only (Husson et al., 2018). Fast subsidence in the Gippsland Basin, to the north east of Melbourne, is explained by mining and other extractions (oil, gas, water) (Ng et al., 2015). The joint inversion yields highly uncertain results, that additionally indicate fast uplift in the north. This pattern is not revealed by TG but likely by a few GPS stations only. This result is at odds with the initial interpretation of (Husson et al., 2018) who considered trends of VLM derived from the entire duration of GPS time series. The joint inversion therefore mostly reveals the rates of GSL change, partly corrupted by a few GPS stations. This is demonstrated by the posterior distribution on virtual tide gauges in Figure 7d, which is larger than with TG only (see supporting information). As opposed to the typical case of South America where TG are scarce, here our joint inversion yields predictions that are more difficult to interpret, because TG are numerous and a few outliers in GPS stations erroneously dominate the signal. When compared to the earlier studies of Choblet et al. (2014) and Husson et al. (2018), the case of Australia highlights the compromise in time period selection resulting in unsatisfactory results.
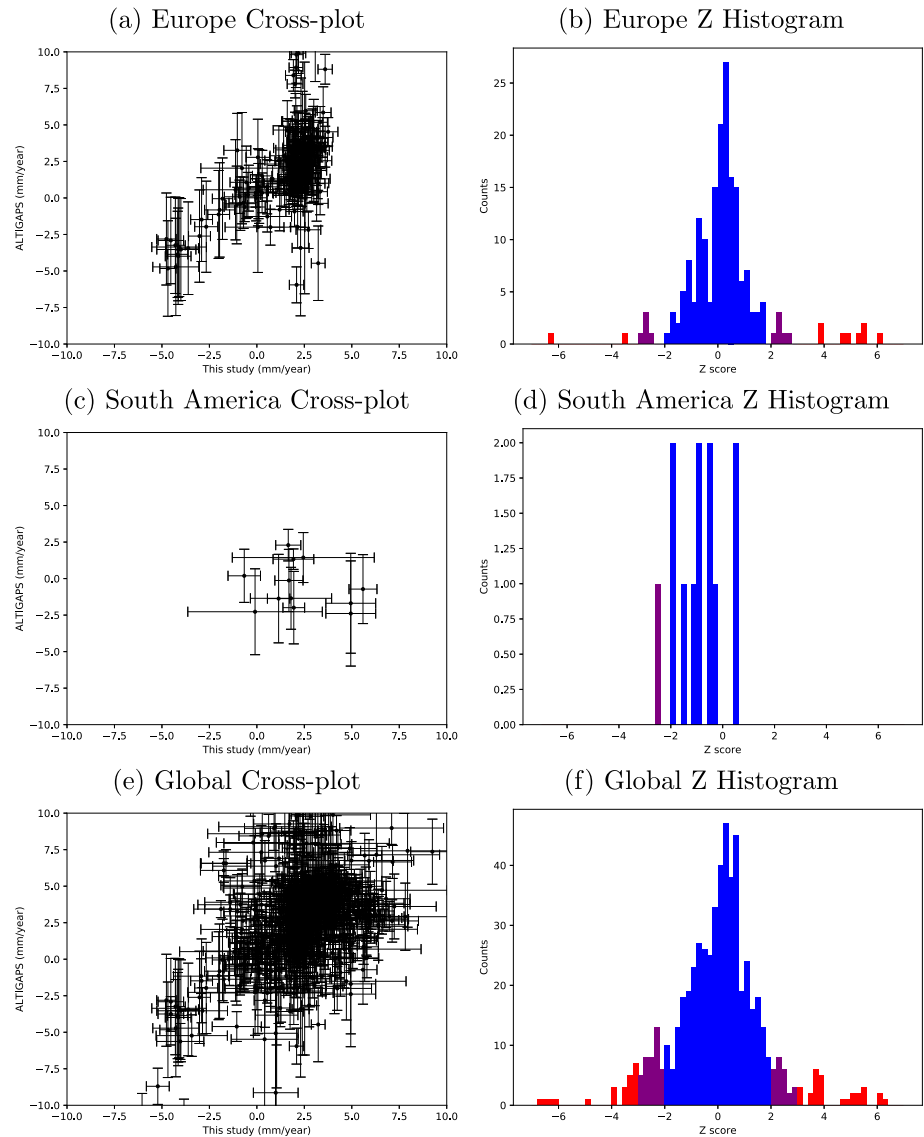
Figure 9. The same plots as in Figure 8; however, this is for the joint inversion without using tide gauges. The results are still in good agreement with ALTIGAPS, and this suggests that with our method, we can predict RSL in locations without nearby tide gauges albeit with higher uncertainties as shown in the posterior plots (e.g., Figures 3 and 5).

5. Comparison With ALTIGAPS

As a validation of our approach we can compare our predictions against those of the ALTIGAPS data set (Pfeffer and Allemand, 2016). ALTIGAPS contains estimates of RSL rise at selected TG across the globe corrected for VLM and GSL using nearby GPS and SRA data. We use similar data; however, we generate regional maps which we can then interogate rates and uncertainties at points of interest.

In Figure 8 we show cross-plots and Z score histograms for the predictions of ALTIGAPS versus our inversions using all three classes of observations. Cross-plots simply plot two data predictions against each other so agreement between the two ideally should result in a linear trend. The Z score between two predictions $\mu_1 \pm \sigma_1$ and $\mu_2 \pm \sigma_2$ is given by

$$Z = \frac{\mu_1 - \mu_2}{\sqrt{\sigma_1^2 + \sigma_2^2}}. \tag{6}$$

Under the assumption that errors follow a normal distribution, we consider a *Z* score with magnitude greater than three as a disagreement between RSL estimates. A magnitude between 2 and 3 is marginal and less than two is in good agreement.

In Figure 8a we can see that for the European region where there are a large number of TG, the two predictions are in good agreement as evidenced by the near linear relationship. In Figure 8b, the *Z* score histogram for Europe shows only a small number of stations (13 in red shading out of 187) where there is significant disagreement. The good agreement between ALTIGAPS and this study is perhaps unsurprising since they use similar source data although at different time periods. However, there is an important distinction, our method takes into account spatial correlation between TG, GPS, and SRA whereas ALTIGAPS treats each TG independently (comparisons between the raw TG data, ALTIGAPS and this study are shown in Appendix B for some of the TG stations where the results are in disagreement). For South America, there are very few tide gauges in the ALTIGAPS database; hence, a linear trend in the cross-plot in Figure 8c is inconclusive. In Figure 8d, all the predictions between the two methods are in good agreement for South America. When we include all the results from the six study regions (covering 584 of 628 ALTIGAPS data points), we can see in Figures 8e and 8f that the two results are in agreement.

In order to further explore the predictive ability of virtual tide gauges, a more insightful comparison is to compare ALTIGAPS (with all three data sets) to the inversions where only GPS and SRA are used, that is, a leave one data set out cross-validation test. In Figure 9 we show the comparable cross-validation plots of our inversions without TG versus ALTIGAPS. As can be seen, the plots are almost identical to those in Figure 8. This demonstrates that our method can robustly estimate RSL rates using only virtual tide gauges from SRA and GPS and can used to provide RSL estimates in regions without sufficient TG coverage (and complementary observations where TG coverage is good).

6. Conclusions

We have presented a new joint surface reconstruction for rates of GSL change, VLM and RSL change using recent time series observations from tide gauges (TG), GPS and satellite radar altimetry (SRA). We demonstrated that the Bayesian approach can provide probabilistic estimates of RSL rates along shorelines, including estimates of uncertainties, when at least two data sets are sufficiently dense.

We compared results obtained by inverting all three data sets against results obtained from only TG observations, or only GPS and SRA observations. These tests demonstrate that a joint inversion of all available data provides the best overall constraint (i.e., the lowest posterior uncertainties). However, using only GPS and SRA observations to estimate RSL rates at shorelines is highly comparable to our full joint inversion of all data types.

In regions where historical tide gauge emplacement is poor, yet GPS stations are available, reliable estimates of RSL change are possible with our new approach with what we refer to as virtual tide gauges. We demonstrated this with a regional study in South America where tide gauge coverage is sparse yet GPS coverage is more regular.

Importantly, the spatial distribution and density of TG and GPS data is critical for uncertainties and resolution. This is well illustrated by scrutinizing the variety of model responses to several regions examined in this study. For example, in Africa or in the western part of Asia, the data coverage is probably too low for a reliable inversion. In such regions, our results suggest that the deployment of GPS stations near the coast would provide an effective means for obtaining data for future estimates of RSL rise. In the eastern part of Asia, where TG and GPS networks meet the requirements for our inversion procedure, virtual tide gauges improve the estimates of RSL by reducing uncertainties. Europe and North America behave similarly, as they both have dense networks of TG and GPS. Nonetheless, by including GPS and SRA observations, shorter wavelength features are better constrained in the joint inversion than relying only on TG observations.

A comparison was performed against the ALTIGAPS database of RSL rates at TG locations, corrected using GPS and Satellite altimetry (Pfeffer and Allemand, 2016). Our approach, using the joint inversion is in good agreement with the ALTIGAPS database. More importantly, when our approach is used to invert regions for
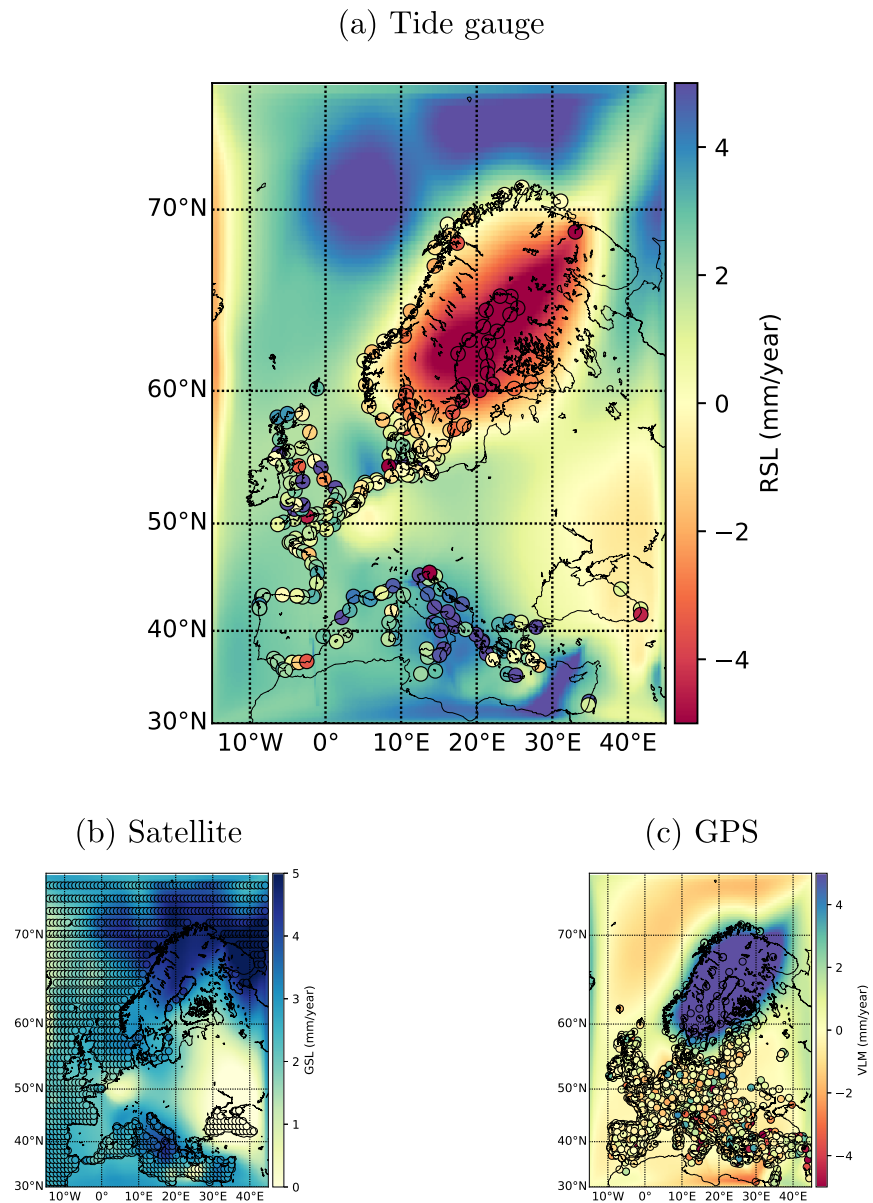
(a) Tide gauge

(b) Satellite

(c) GPS

Figure A1. Scatter plots of the data sets used in the European region inversion with the ensemble mean as background using the same color scale for points and mean. (a) TG/RSL. (b) SRA/GSL. (c) GPS/VLM.

RSL rates with only GPS and satellite data, the results remain compatible with ALTIGAPS, suggesting that robust estimates of RSL rates are possible regardless of the number of neighboring TG.

However, by no means do we suggest that TG are useless: They convey unique information about interannual to multidecadal variability in RSLs and constitute a valuable source of information to study the ocean response to climate change at secular time scales. Tide gauges can also reflect more local changes in coastal sea levels that are not captured by our Bayesian inversion, but that are important to consider when assessing coastal hazards related to RSL rise.

While we have demonstrated the validity of the approach through many tests, we reiterate that our method relies on data quality and distribution. In this study, the data are sensitive to the time period selected and we have chosen some simplifying assumptions in the processing of our data, predominantly related to constant rates (i.e., linear trends) for GSL, VLM, and RSL. All of the observations used in this study depend on a wide variety of climatic, tectonic and human influences that greatly contribute to nonlinear variations in time, thus resulting in uncertainties in our estimates. Such uncertainties are most manifest in local interan-
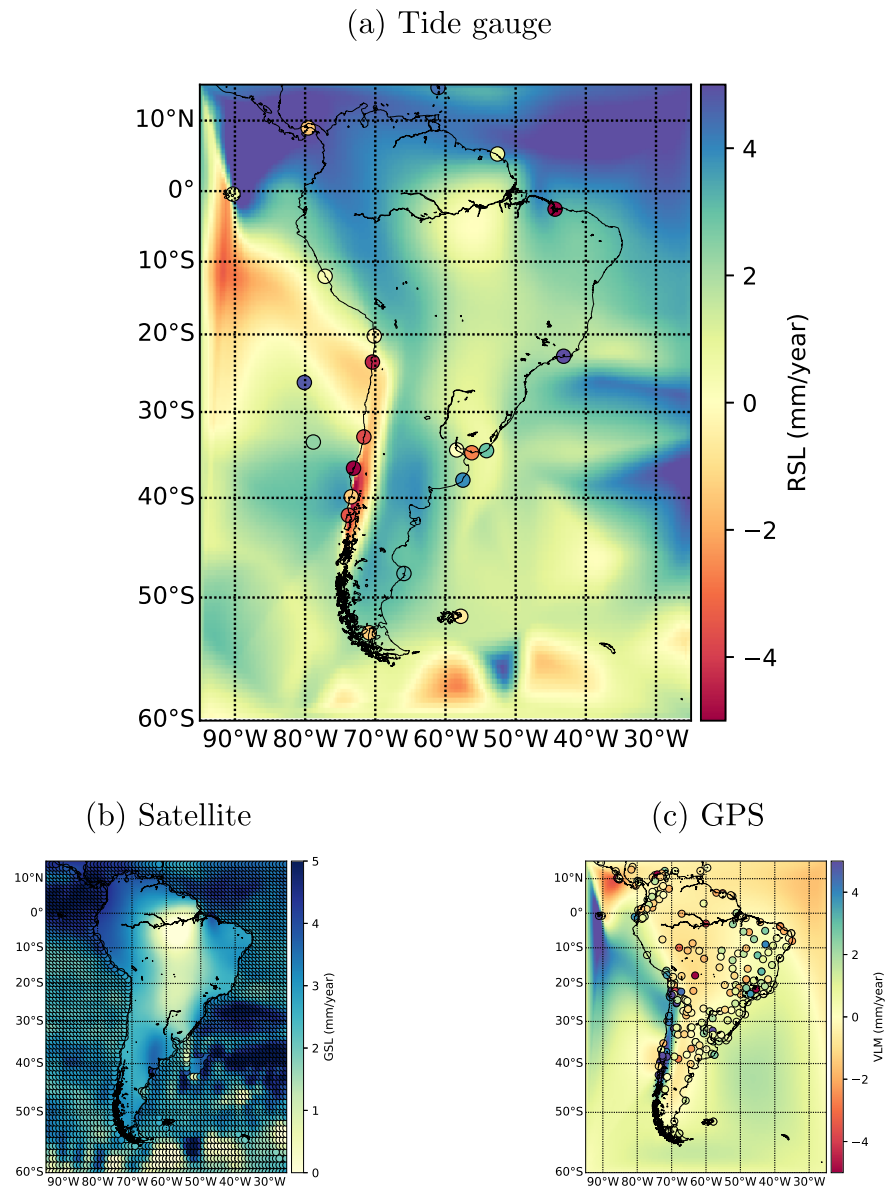
(a) Tide gauge

(b) Satellite

(c) GPS

Figure 2. Scatter plots of the data sets used in the South American region inversion with the ensemble mean as background using the same color scale for points and mean. (a) TG/RSL. (b) SRA/GSL. (c) GPS/VLM.

nual fluctuations of vertical rates in the tide-gauge record. However, generally we find that when assessing regional trends of sea-level variation, virtual tide gauges are less affected by such bias and prove to be a useful means to alleviate the effect of the uncertainties in the trends of RSL directly derived from tide gauges.

Appendix A: A Regional Data Plots

In this section we show the ensemble mean models with over plotted data points for the two regions considered in this manuscript. In Figure A1 for the Europe region and Figure 2 for South America. Plots for other regions appear in the supporting information.

Appendix B: Outliers Versus ALTIGAPS

In Figure B1 we show the raw data used in this study for TG (solid black line) compared against rates predicted by ALTIGAPS (red dashed line) and this study (green dashed line). Also shown is the RSL rate pre-
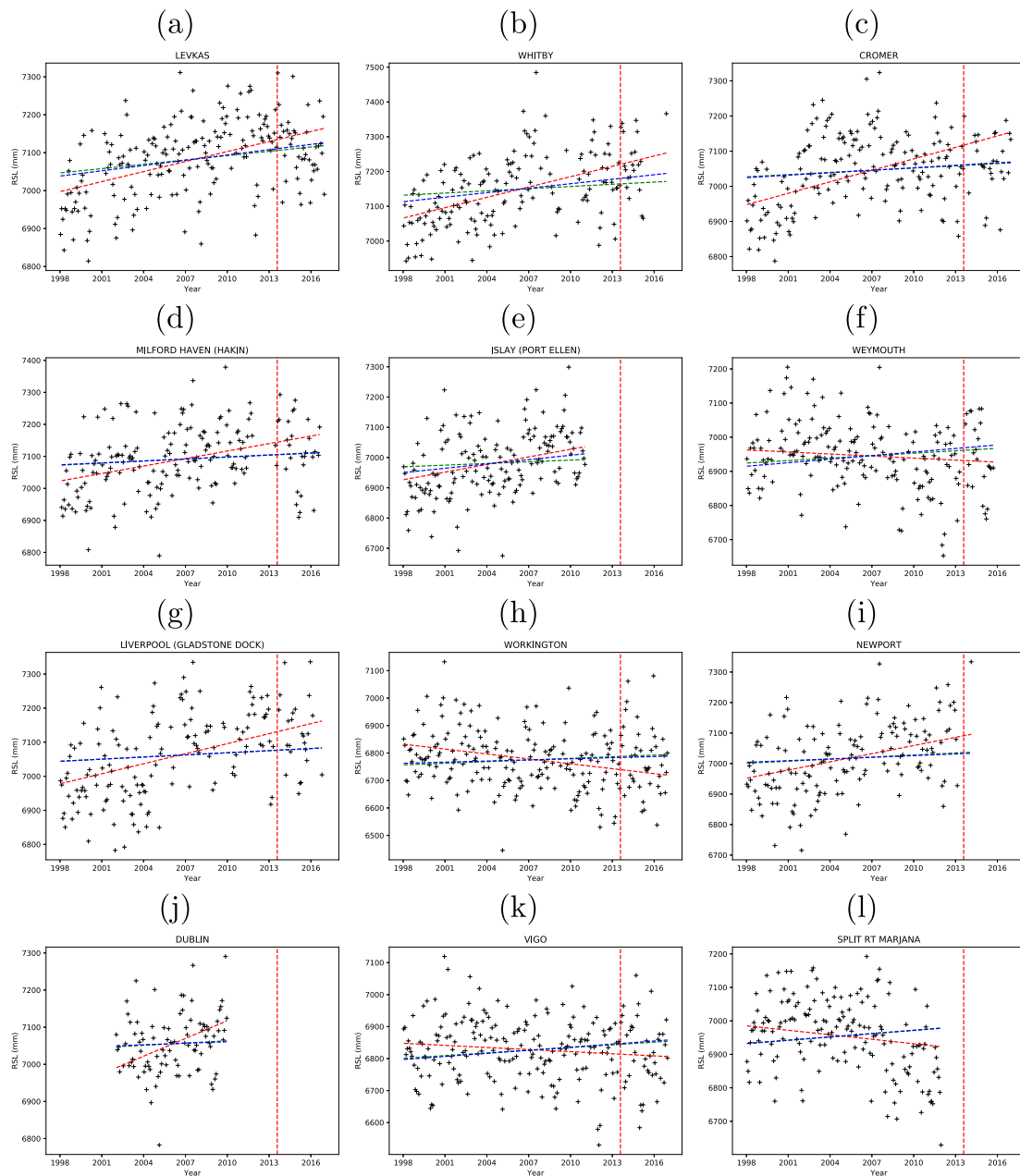
Figure B1. Plots of the ALTIGAPS predictions (red dashed) and this study (green dashed) are shown for 12 stations where there is significant disagreement between RSL predictions. The temporal range of the ALTIGAPS study is indicated with vertical red dashed lines (i.e., 1993 … 2013). The raw monthly tide gauge record is shownwith black points. Also shown with a blue line are the RSL rates predicted by the nearest GSL and VLM observations.

dicted by the nearest SRA observation and nearest GPS observation. We have included 12 of the 13 outliers simply (two not shown for space reasons). In the figure, discrepancies between the two results can sometimes be adequately explained by differences in records, for example, the Weymouth (f) station contains a slight rise in 2016 which may not have been fully included in the ALTIGAPS study. This again highlights the importance of the selection of the time period due to the large variations in TG records.

Many of the TG records appear to have large variability in RSL. Predictions from nearby observations of VLM and GSL rates from which an RSL rate can be predicted (shown in blue) are generally similar to the joint inversion result (green). This suggests that the variability of TG observations is down played in the joint inversions.

References

Aki, K. (1977). Determination of the three-dimensional seismic structure of the lithosphere. *Journal of Geophysical Research*, *82*(2), 277–296. https://doi.org/10.1029/JB082i002p00277

Angelier, J., Cadet, J., Delibrias, G., Fourniguet, J., Gigout, M., Guillemin, M., & Pierre, G. (1976). Les déformations du quaternaire marin, indicateurs néotectoniques. quelques exemples méditerranéens. *Revue de Géographie Physique et de Géologie Dynamique*, *18*, 427–488.

Backus, G., & Gilbert, F. (1968). The resolving power of gross Earth data. *Geophysical Journal of the Royal Astronomical Society*, *16*(2), 169–205. https://doi.org/10.1111/j.1365-246X.1968.tb00216.x

Blewitt, G., Kreemer, C., Hammond, W. C., & Gazeaux, J. (2015). MIDAS robust trend estimator for accurate GPS station velocities without step detection. *Journal of Geophysical Research: Solid Earth*, *121*, 2054–2068. https://doi.org/10.1002/2015JB012552

Bosch, W., Dettmering, D., & Schwatke, C. (2014). Multi-mission cross-calibration of satellite altimeters: Constructing a long-term data record for global and regional sea level change studies. *Remote Sensing*, *6*(3), 2255–2281. https://doi.org/10.3390/rs6032255

Bouin, M. N., & Wöppelmann, G. (2010). Land motion estimates from GPS at tide gauges: A geophysical evaluation. *GJI*, *180*(1), 193–209.

Brooks, S., Gelman, A., Jones, G. L., & Meng, X. (2011). *Handbook of Markov chain Monte Carlo*. Boca Raton, Florida: Chapman and Hall/CRC. https://doi.org/10.1201/b10905

Carrère, L., Faugère, Y., & Ablain, M. (2016). Major improvement of altimetry sea level estimations using pressure-derived corrections based on ERA-Interim atmospheric reanalysis. *Ocean Science*, *12*(3), 825–842. https://doi.org/10.5194/os-12-825-2016

Carrère, L., & Lyard, F. (2003). Modeling the barotropic response of the global ocean to atmospheric wind and pressure forcing-comparisons with observations. *Geophysical Research Letters*, *30*(6), 1275. https://doi.org/10.1029/2002GL016473

Cazenave, A., & Cozannet, G. L. (2014). Sea level rise and its coastal impacts. *Earth's Future*, *2*, 15–34. https://doi.org/10.1002/2013EF000188

Cazenave, A., & Palanisamy, H. (2018). *Global change and future Earth: The geoscience perspective* (Vol. 3, p. 144). Cambridge: Cambridge University Press.

Chen, X., Zhang, X., Church, J. A., Watson, C. S., King, M. A., Monselesan, D., & Harig, C. (2017). The increasing rate of global mean sea-level rise during 1993–2014. *Nature Climate Change*, *7*(7), 492–495. https://doi.org/10.1038/nclimate3325

Choblet, G., Husson, L., & Bodin, T. (2014). Probabilistic surface reconstruction of coastal sea level rise during the twentieth century. *Journal of Geophysical Research: Solid Earth*, *119*, 9206–9236. https://doi.org/10.1002/2014JB011639

Church, J. A., Clark, P. U., Cazenave, A., Gregory, J. M., Jevrejeva, S., Levermann, A., & Unnikrishnan, A. S. (2013). Climate change 2013: The physical science basis. Contribution of Working Group I to the Fifth Assessment Report of the Intergovernmental Panel on Climate Change. In T. F. Stocker et al. (Eds.), *Sea level change [Book Section]* (pp. 1137–1216). Cambridge: Cambridge University Press.

Church, J. A., & White, N. J. (2011). Sea-level rise from the late 19th to the early 21st century. *Surveys in Geophysics*, *32*(4-5), 585–602. https://doi.org/10.1007/s10712-011-9119-1

Church, J. A., White, N. J., Coleman, R., Lambeck, K., & Mitrovica, J. X. (2004). Estimates of the regional distribution of sea level rise over the 1950–2000 period. *Journal of Climate*, *17*(13), 2609–2625. https://doi.org/10.1175/1520-0442(2004)017<2609:EOTRDO>2.0.CO;2

Clark, P. U., Mitrovica, J. X., Milne, G. A., & Tamisiea, M. E. (2002). Sea-level fingerprinting as a direct test for the source of global meltwater pulse IA. *Science*, *295*(5564), 2438–2441. https://doi.org/10.1126/science.1069017

Conrad, C. P. (2013). The solid Earth's influence on sea level. *GSA Bulletin*, *125*(7-8), 1027–1052. https://doi.org/10.1130/B30764

Copernicus Marine and Environment Monitoring Service (2018). MSLA—Monthly mean and climatology maps of sea level anomalies. (data retrieved from Aviso, https://www.aviso.altimetry.fr/en/data/products/sea-surface-height-products/global/msla-mean-climatology.html)

Dangendorf, S., Marcos, M., Wöppelmann, G. P., Conrad, C., Frederikse, T., & Riva, R. (2017). Reassessment of 20th century global mean sea level rise. *Proceedings of the National Academy of Sciences*, *114*(23), 5946–5951. https://doi.org/10.1073/pnas.1616007114

Dee, D. P., Uppala, S. M., Simmons, A. J., Berrisford, P., Poli, P., Kobayashi, S., & Vitart, F. (2011). The ERA-Interim reanalysis: Configuration and performance of the data assimilation system. *Quarterly Journal of the Royal Meteorological Society*, *137*(656), 553–597. https://doi.org/10.1002/qj.828

Dieng, H. B., Cazenave, A., Meyssignac, B., & Ablain, M. (2017). New estimate of the current rate of sea level rise from a sea level budget approach. *Geophysical Research Letters*, *44*, 3744–3751. https://doi.org/10.1002/2017GL073308

Douglas, B. C. (1992). Global sea level acceleration. *Journal of Geophysical Research*, *97*(C8), 12,699–12,706. https://doi.org/10.1029/92JC01133

Duane, S., Kennedy, A. D., Pendelton, B. J., & Roweth, D. (1987). Hybrid Monte Carlo. *Physics Letters B*, *195*(2), 216–222. https://doi.org/10.1016/0370-2693(87)91197-X

Earl, D. J., & Deem, M. W. (2005). Parallel tempering: Theory, applications, and new perspectives. *Physical Chemistry Chemical Physics*, *7*(23), 3910–3916. https://doi.org/10.1039/b509983h

Featherstone, W. E., Penna, N. T., Filmer, M. S., & Williams, S. D. P. (2015). Nonlinear subsidence at Fremantle, a long-recording tide gauge in the Southern Hemisphere. *Journal of Geophysical Research: Oceans*, *120*, 7004–7014. https://doi.org/10.1002/2015JC011295

Fu, L. L., & Cazenave, A. (2000). Satellite altimetry and Earth sciences: A handbook of techniques and applications. *Elsevier.*, *69*.

Gelman, A., Carlin, J. B., Hal, S., & Rubin, D. B. (2004). *Bayesian data analysis* (2nd ed.). New York: CRC Press.

Gelman, A., & Rubin, D. B. (1992). Inference from iterative simulation using multiple sequences. *Statistical Science*, *7*(4), 457–472. https://doi.org/10.1214/ss/1177011136

Gommenginger, C., Thibaut, P., Fenoglio-Marc, L., Quartly, G., Deng, X., Gómez-Enri, J., & Gao, Y. (2011). RetrackingAltimeter Waveforms Near the Coasts. In S. Vignudelli, A. Kostianoy, & P. Cipollini (Eds.), *Coastal altimetry* (Chap. 4, pp. 61–102). Berlin: Springer. https://doi.org/10.1007/978-3-642-12796-0_4.

Gregory, J. M., Griffies, S. M., Hughes, C. W., Lowe, J. A., Church, J. A., Fukimori, I., & van de Wal, R. S. W. (2019). Concepts and terminology for sea level mean, variability and change, both local and global. *Surveys of Geophysics*, 1–39.

Han, W., Meehl, G. A., Stammer, D., Hu, A., Hamlington, B., Kenigson, J., & Thompson, P. (2017). Spatial patterns of sea level variability associated with natural internal climate modes. In *Integrative study of the mean sea level and its components* (pp. 221–254). Springer.

Hawkins, R., Bodin, T., Sambridge, M., Choblet, G., & Husson, L. (2019). Trans-dimensional surface reconstruction with different classes of parameterization. *Geochemistry, Geophysics, Geosystems*, *20*, 505–529. https://doi.org/10.1029/2018GC008022

Hawkins, R., Brodie, R., & Sambridge, M. (2018). Bayesian trans-dimensional inversion of airborne electromagnetic 2D conductivity profiles. *Exploration Geophysics*, *49*(2), 134–147. https://doi.org/10.1071/EG16139

Hay, C. C., Morrow, E., Kopp, R. E., & Mitrovica, J. X. (2015). Probabilistic reanalysis of twentieth-century sea-level rise. *Nature*, *517*(7535), 481–484. https://doi.org/10.1038/nature14093

Holgate, S. J., Matthews, A., Woodworth, P. L., Rickards, L. J., Tamisiea, M. E., Bradshaw, E., & Pugh, J. (2013). New data systems and products at the permanent service for mean sea level. *Journal of Coastal Research*, *29*(3), 493. https://doi.org/10.2112/JCOASTRES-D-12-00175.1

Horton, B. P., Kopp, R. E., Garner, A. J., Hay, C. C., Khan, N. S., Roy, K., & Shaw, T. A. (2018). Mapping sea-level change in time, space, and probability. *Annual Review of Environment and Resources*, *43*(1), 481–521. https://doi.org/10.1146/annurev-environ-102017-025826

Husson, L., Bodin, T., Spada, G., Choblet, G., & Kreemer, C. (2018). Bayesian surface reconstruction of geodetic uplift rates: Mapping the global fingerprint of GIA. *Journal of Geodynamics*, *122*, 25–40. https://doi.org/10.1016/j.jog.2018.10.002

Husson, L., & Conrad, C. P. (2006). Tectonic velocities, dynamic topography, and relative sea level. *Geophysics Research Letters*, *33*, L18303. https://doi.org/10.1029/2006GL026834

Jevrejeva, S., Grinsted, A., Moore, J. C., & Holgate, S. (2006). Nonlinear trends and multiyear cycles in sea level records. *Journal of Geophysical Research*, *111*, C09012. https://doi.org/10.1029/2005JC003229

Johansson, J. M., Davis, J. L., Scherneck, H. G., Milne, G. A., Vermeer, M., Mitrovica, J. X., & Shapiro, I. I. (2002). Continuous GPS measurements of postglacial adjustments in Fennoscandia 1. *Geodetic results. Journal of Geophysical Research*, *107*(B8).

Kingdom and New York, NY, USA: Cambridge University Press. Retrieved from www.climatechange2013.org https://doi.org/10.1017/CBO9781107415324.026

Klos, A., Kusche, J., Fenoglio-Marc, L., Bos, M. S., & Bogusz, J. (2019). Introducing a vertical land motion model for improving estimates of sea level rates derived from tide gauge records affected by earthquakes. *GPS Solutions*, *23*(4), 102. https://doi.org/10.1007/s10291-019-0896-1

Köhl, A., & Stammer, D. (2008). Decadal sea level changes in the 50-year GECCO ocean synthesis. *Journal of Climate*, *21*(9), 1876–1890. https://doi.org/10.1175/2007JCLI2081.1

Kreemer, C., Hammond, W. C., & Blewitt, G. (2018). A robust estimation of the 3-D intraplate deformation of the North American plate from GPS. *Journal of Geophysical Research: Solid Earth*, *123*, 4388–4412. https://doi.org/10.1029/2017JB015257

Lambeck, K., & Johnston, P. (1998). The Viscosity of the Mantle: Evidence from Analyses ofGlacial-Rebound Phenomena. In I. Jackon (Ed.), *The Earth's mantle* (pp. 461–502). Cambridge: Cambridge University Press.

Lambeck, K., & Purcell, A. (2005). Sea-level change in the Mediterranean sea since the LGM: Model predictions for tectonically stable areas. *Quaternary Science Reviews*, *24*(18-19), 1969–1988. https://doi.org/10.1016/j.quascirev.2004.06.025

Legeais, J.-F., Ablain, M., Zawadzki, L., Zuo, H., Johannessen, J. A., Scharffenberg, M. G., & Benveniste, J. (2018). An improved and homogeneous altimeter sea level record from the ESA Climate Change Initiative. *Earth System Science Data*, *10*(1), 281–301. https://doi.org/10.5194/essd-10-281-2018

Lombard, A., Garric, G., & Penduff, T. (2009). Regional patterns of observed sea level change: Insights from a 1/4° global ocean/sea-ice hindcast. *Ocean Dynamics*, *59*(3), 433–449. https://doi.org/10.1007/s10236-008-0161-6

Malinverno, A. (2002). Parsimonious Bayesian Markov chain Monte Carlo inversion in a nonlinear geophysical problem. *Geophysical Journal International*, *151*(3), 675–688. https://doi.org/10.1046/j.1365-246X.2002.01847.x

Malinverno, A., & Briggs, V. A. (2004). Expanded uncertainty quantification in inverse problems: Hierarchical Bayes and empirical Bayes. *Geophysics*, *69*(4), 1005–1016. https://doi.org/10.1190/1.1778243

Menke, W., & Blatter, D. (2019). Trade-off of resolution and variance computed from ensembles of solutions, with application to Markov Chain Monte Carlo methods. *Geophysical Journal International*, *218*(3), 1522–1536. https://doi.org/10.1093/gji/ggz245

Milne, G. A., Davis, J. L., Mitrovica, J. X., Scherneck, H. G., Johansson, J. M., Vermeer, M., & Koivula, H. (2001). Space-geodetic constraints on glacial isostatic adjustment in Fennoscandia. *Science*, *291*(5512), 2381–2385. https://doi.org/10.1126/science.1057022

Mitrovica, J. X., Milne, G. A., & Davis, J. L. (2001). Glacial isostatic adjustment on a rotating Earth. *GJI*, *147*(3), 562–578.

Mosegaard, K., & Tarantola, A. (1995). Monte Carlo sampling of solutions to inverse problems. *Journal of Geophysical Research*, *100*(B7), 12,431–12,447. https://doi.org/10.1029/94JB03097

Neal, R. M. (2011). MCMC UsingHamiltonian Dynamics. In *Handbook of Markov chain Monte Carlo*. Boca Raton, Florida: Chapman and Hall/CRC. https://doi.org/10.1201/b10905-6

Nerem, R. S., Beckley, B. D., Fasullo, J. T., Hamlington, B. D., Masters, D., & Mitchum, G. T. (2018). Climate-change driven accelerated sea-level rise detected in the altimeter era. *Proceedings of the National Academy of Sciences*, *115*(9), 2022–2025. https://doi.org/10.1073/pnas.1717312115

Ng, A. H. M., Ge, L., & Li, X. (2015). Assessments of land subsidence in the Gippsland basin of Australia using ALOS PALSAR data. *Remote Sensing of Environment*, *159*, 86–101. https://doi.org/10.1016/j.rse.2014.12.003

Pascual, A., Marcos, M., & Gomis, D. (2008). Comparing the sea level response to pressure and wind forcing of two barotropic models: Validation with tide gauge and altimetry data. *Journal of Geophysical Research*, *113*, C07011. https://doi.org/10.1029/2007JC004459

Peltier, W. R. (1998). Postglacial variations in the level of the sea: Implications for climate dynamics and solid-Earth geophysics. *Reviews of Geophyics*, *36*(4), 603–689. https://doi.org/10.1029/98RG02638

Peltier, W. R., & Andrews, J. T. (1976). Glacial-Isostatic Adjustment—I. The forward problem. *Geophysical Journal of the Royal Astronomical Society*, *46*(3), 605–646. https://doi.org/10.1111/j.1365-246X.1976.tb01251.x

Pfeffer, J., & Allemand, P. (2016). The key role of vertical land motions in coastal sea level variations: A global synthesis of multisatellite altimetry, tide gauge data and GPS measurements. *Earth and Planetary Science Letters*, *439*, 39–47. https://doi.org/10.1016/j.epsl.2016.01.027

Pfeffer, J., Spada, G., Mémin, A., Boy, J.-P., & Allemand, P. (2017). Decoding the origins of vertical land motions observed today at coasts. *Geophysical Journal International*, *210*(1), 148–165. https://doi.org/10.1093/gji/ggx142

Pfeffer, J., Tregoning, P., Purcell, A., & Sambridge, M. (2018). Multitechnique assessment of the interannual to multidecadal variability in steric sea levels: A comparative analysis of climate mode fingerprints. *Journal of Climate*, *31*(18), 7583–7597. https://doi.org/10.1175/JCLI-D-17-0679.1

Quigley, M. C., Clark, D., & Sandiford, M. (2010). Tectonic geomorphology of Australia. *Geological Society, London, Special Publications*, *346*(1), 243–265. https://doi.org/10.1144/SP346.13

Richter, A., Ivins, E., Lange, H., Mendoza, L., Schröder, L., Hormaechea, J., & Dietrich, R. (2016). Crustal deformation across the southern Patagonian icefield observed by GNSS. *Earth and Planetary Science Letters*, *452*, 206–215. https://doi.org/10.1016/j.epsl.2016.07.042

Rignot, E., Velicogna, I., van den Broeke, M. R., Monaghan, A., & Lenaerts, J. T. M. (2011). Acceleration of the contribution of the Greenland and Antarctic ice sheets to sea level rise. *Geophysical Research Letters*, *38*, L05503. https://doi.org/10.1029/2011GL046583

Rovere, A., Stocchi, P., & Vacchi, M. (2016). Eustatic and relative sea level changes. *Current Climate Change Reports*, *2*(4), 221–231. https://doi.org/10.1007/s40641-016-0045-7

Sambridge, M. (2014). A parallel tempering algorithm for probabilistic sampling and multimodal optimization. *Geophysical Journal International*, *192*, 357–374.

Sambridge, M., & Mosegaard, K. (2002). Monte Carlo methods in geophysical inverse problems. *Reviews of Geophysics*, *40*(3), 1–29.

Sandiford, M., Coblentz, D., & Schellart, W. P. (2005). Evaluating slab-plate coupling in the Indo-Australian plate. *Geology*, *33*(2), 113. https://doi.org/10.1130/G20898.1

Smith-Konter, B. R., Thornton, G. M., & Sandwell, D. T. (2014). Vertical crustal displacement due to interseismic deformation along the San Andreas fault: Constraints from tide gauges. *Geophysical Research Letters*, *41*, 3793–3801. https://doi.org/10.1002/2014GL060091

Stammer, D., Cazenave, A., Ponte, R. M., & Tamisiea, M. E. (2013). Causes for contemporary regional sea level changes. *Annual Review of Marine Science*, *5*(1), 21–46. https://doi.org/10.1146/annurev-marine-121211-172406

Watson, C. S., White, N. J., Church, J. A., King, M. A., Burgette, R. J., & Legresy, B. (2015). Unabated global mean sea-level rise over the satellite altimeter era. *Nature Climate Change*, *5*(6), 565–568. https://doi.org/10.1038/nclimate2635

WCRP Global Sea Level Budget Group (2018). Global sea-level budget 1993–present. *Earth System Science Data*, *10*(3), 1551–1590. https://doi.org/10.5194/essd-10-1551-2018

Woodworth, P. L., & Player, R. (2003). The permanent service for mean sea level: An update to the 21st century. *Journal of Coastal Research*, 287–295.

Woppelmann, G., & Marcos, M. (2016). Vertical land motion as a key to understanding sea level change and variability. *Reviews of Geophysics*, *54*, 64–92. https://doi.org/10.1002/2015RG000502

Yagi, Y., & Fukahata, Y. (2011). Rupture process of the 2011 Tohoku-oki earthquake and absolute elastic strain release. *Geophysical Research Letters*, *38*, L19307. https://doi.org/10.1029/2011GL048701